Curvature and pressure-gradient effects on a small-defect wake

Nakayama, A.

(Citation)
Journal of Fluid Mechanics,175:215-246

(Issue Date)
1987-02

(Resource Type)
journal article

(Version)
Version of Record

(URL)
https://hdl.handle.net/20.500.14094/90001182

J. Fluid Mech. (1987), *vol.* 175, *pp.* 215–246
Printed in Great Britain

Curvature and pressure-gradient effects on a small-defect wake

By A. NAKAYAMA

Aerodynamics Research and Technology Department, Douglas Aircraft Company, Long Beach, CA 90846, USA

(Received 5 August 1985 and in revised form 19 June 1986)

A fully developed two-dimensional turbulent wake was deflected by an airfoil-like thin plate placed at small angles in the external flow. The response of the mean-flow and turbulence properties of the wake to the 'mild' pressure gradient and the 'mild' streamline curvature caused by the deflection is studied. Owing to the small defect velocity, the extra strain rates are large compared with the main shear strain and the Reynolds stresses are strongly influenced by both the pressure gradient and the streamline curvature. The defect velocity relative to an appropriately chosen 'potential-flow velocity', and the mean vorticity, however, are not as strongly influenced by the curvature. Changes in the magnitudes of the Reynolds-stress components are much larger than would be caused by the simple rotation of coordinates aligned with the wake path. Most turbulence-model parameters are influenced significantly, while some pure turbulence parameters, such as the Taylor microscale, are relatively uninfluenced. The rapid and lagged responses are apparent and the terms in the transport equation for turbulent kinetic energy indicate that the response of the production terms is almost instantaneous, while the diffusion and dissipation terms are delayed.

1. Introduction

Characteristics of a plane wake with a small velocity deficit, such as the far wake of a two-dimensional obstacle, are expected to be sensitive to relatively small perturbations in an otherwise uniform external flow since the wake decay is dictated by the shear stress, which is proportional to the square of the *defect* velocity, and can be much smaller than the perturbations in pressure or inertia forces, which are proportional to the square of the *total* velocity. Although the overall mean-flow quantities may be explained by an inviscid model, as in the case of a strong distortion in a moderate-depth wake considered by Hill, Schaub & Senoo (1963), quantities that are related to the turbulence, such as the decay and spread, still need to be explained by considering the turbulent stresses. The examination of the response of the turbulent stresses to small distortions of the external flow is the main subject of this paper.

In small-defect wakes, where the transverse variation of the velocity is much smaller than the absolute value, the ratio of the extra rate of strain due to the streamline curvature $\partial V/\partial x$ to the main shear $\partial U/\partial y$ can be very large in apparently mildly curving wakes (i.e. small δ/R where δ is a measure of wake width and R is the local radius of streamline curvature). This implies that small curvature may induce changes in the turbulence quantities, which is in contrast to curved shear layers where the minimum velocity is zero or near zero, such as wall-bounded shear layers, single-stream mixing layers and jets in still ambient fluid. For the same reason,

small streamwise pressure gradients can also influence the evolution of the turbulent stresses. The fact that the outer parts of boundary layers have many features in common with wakes, and that it is in this part that the curvature effects are felt most strongly, suggests a strong sensitivity of wakes to streamline curvatures.

Understanding of perturbed small-defect wakes is very important in advancing methods for analysing and predicting various wake flows of practical importance. Experimental data are needed for this purpose, and to verify turbulence models such as the transport-equation models of Launder, Reece & Rodi (1975) and Gibson & Rodi (1981) and of the rapid-distortion models of Hunt (1978), Savill (1982) and Townsend (1980). Despite the importance of the problem and the above-described special features, there are not enough detailed data on wakes asymmetrically distorted by the external flows.

Studies of streamline-curvature effects on wakes have recently been reported by Koyama (1983) and Savill (1983). Koyama (1983) investigated the mean and turbulence properties of the initial developing part of a cylinder wake developing in a curved channel in the absence of a streamwise pressure gradient. The flow in this region is influenced strongly by the vortex shedding, and the turbulence mechanisms are different from those in the developed wake. Savill (1983) investigated a cylinder wake that is turned by as much as 90° by means of a back plate so that it is both highly curved and influenced by a streamwise pressure gradient. The data indicate the strong influence of the streamline curvature on the wake, and that the turbulent-stress fields are complex owing to the coexistence of the stabilized and destabilized regions across the wake and the interaction between them.

The present study documents the effects of mild streamline curvature on the mean and turbulence quantities of a fully developed plane wake. The wake curvature is achieved by means of a thin plate placed near, but outside, the wake at a small angle to the undisturbed free-stream direction, as shown in figure 1. As in the case of Savill (1983), there is an effect of streamwise pressure gradient as well as streamline curvature and the existence of the former makes it difficult to examine the latter because they interact (Smits, Young & Bradshaw 1979; Smits & Joubert 1981; Smits & Wood 1985). In the present study, qualitative separation of the two effects is possible since two wakes were investigated, formed by placing the wake-deflection plate at positive and negative angles as indicated in figure 1. The two wakes curve in opposite directions while in almost opposite streamwise pressure gradients, so that pressure-gradient effects are manifested by opposite trends between the two cases, while streamline curvature effects are indicated by antisymmetric flow features. Since the wake deflection is introduced after the flow reaches full development, the effects of the extra strain rates can easily be distinguished as in the case of more basic homogeneous shear flow of Sreenivasan (1983).

Investigations are centred around the region where the wake curves, and encompass the initial response and initial recovery back to a straight wake. Among many published works on curvature effects, some of those that relate to the present work are the measurements of Castro & Bradshaw (1976) made in a curved mixing layer, Smits *et al.* (1979), Smits & Joubert (1981), Gillis & Johnston (1983) and Muck, Hoffman & Bradshaw (1985) made on boundary layers with curvature effects.

2. Small-defect wake with mild pressure gradient and curvature

In this section, equations of motion are derived that describe the small-defect wake with a mild pressure gradient and mild curvature.

In curvilinear coordinates (s, n), where s is the distance along a streamline near the wake centre (to be defined below) and n is the normal distance from this streamline, the continuity and momentum equations, omitting the viscous terms for high-Reynolds-number flows, are

$$\frac{\partial U}{\partial s}+\frac{\partial}{\partial n}\left[\left(1+\frac{n}{R}\right)V\right]=0, \tag{1}$$

$$\frac{U}{1+n/R}\frac{\partial U}{\partial s}+V\frac{\partial U}{\partial n}+\frac{UV}{R(1+n/R)}=-\frac{1}{1+n/R}\frac{1}{\rho}\frac{\partial p}{\partial s}-\frac{1}{1+n/R}\frac{\partial}{\partial s}\overline{u^2}$$
$$-\frac{\partial}{\partial n}\overline{uv}-\frac{2\overline{uv}}{R(1+n/R)}, \tag{2}$$

$$\frac{U}{1+n/R}\frac{\partial V}{\partial s}+V\frac{\partial V}{\partial n}-\frac{U^2}{R(1+n/R)}=-\frac{1}{\rho}\frac{\partial p}{\partial n}-\frac{\partial}{\partial n}\overline{v^2}-\frac{1}{1+n/R}\frac{\partial}{\partial s}\overline{uv}+\frac{\overline{u^2}-\overline{v^2}}{R}, \tag{3}$$

where $R(s)$ is the local radius of the curvature of the streamline $n = 0$, taken to be positive if convex in the positive-n direction. We then assume the following order-of-magnitude relations for a small-defect wake with mild pressure gradient and mild curvature:

$$\frac{U_s}{U_1}\approx\frac{\delta}{L}\approx\frac{\delta}{R}\ll 1, \tag{4}$$

where U_1 is the velocity outside the wake, U_s is the maximum variation of the velocity across the wake, L is the streamwise lengthscale, and δ is half the wake thickness. The special feature of the conditions considered here, compared with those of the curved shear layers studied, for example, by Margolis & Lumley (1965) and Castro & Bradshaw (1976) in the mixing layer, and by Guitton & Newman (1977) in the curved wall jet, is derived from the 'small-defect' assumption $U_s/U_1 \ll 1$. When $U_s/U_1 \ll 1$, the basic conditions, $\delta/L \ll 1$ and $\delta/R \ll 1$ for the boundary-layer approximation do not lead to such consequences as $\partial U/\partial n \gg \partial U/\partial s$. In fact, $\partial U/\partial n = O(U_s/\delta)$ and $\partial U/\partial s = O(U_1/L) = O(U_s/\delta)$ so that $\partial U/\partial n$ and $\partial U/\partial s$ are of the same order of magnitude.

Equations are now simplified under the above-described conditions. The continuity equation (1) reduces to

$$\frac{\partial U}{\partial s}+\frac{\partial V}{\partial n}=0, \tag{5}$$

which implies that V is of the order of $U_1\delta/L$, and $V \ll U$ so that the flow may still be classified as almost unidirectional like many other thin shear layers. The scale of velocity fluctuation, like other turbulent shear flows, is U_s and the turbulent correlation terms are of the order of U_s^2. Then the terms of largest order in the y-component equation (3) are

$$-\frac{U^2}{R}=-\frac{1}{\rho}\frac{\partial p}{\partial n}, \tag{6}$$

which, after integration, gives the pressure

$$\frac{p}{\rho}=\frac{1}{R}\int_0^n U^2\,\mathrm{d}n+\frac{p_0}{\rho}, \tag{7}$$

where p_0 is the pressure along $n = 0$. This expression is accurate to the order of $U_1^2\delta/R$. Its s-derivative is accurate to the order of $(U_1^2/L)(\delta/R)$, so it can be used in the x-momentum equation to extract an approximation to this order. However, the

largest-order terms in the x-component momentum equation are of the order of U_1^2/L, and if only these terms are retained, we have

$$U\frac{\partial U}{\partial s} = -\frac{1}{\rho}\frac{\partial p}{\partial s}. \tag{8}$$

Equations (5), (6) and (8) represent an inviscid rotational flow.

In order to examine the 'wake' characteristics of the flow, such as the momentum- and mass-flux deficit, the equations must retain terms of one order smaller. To this end, we introduce a hypothetical velocity $U_p(s, n)$ such that

$$\frac{p}{\rho}+\tfrac{1}{2}U_p^2 = \left[\frac{p}{\rho}+\tfrac{1}{2}U^2\right]_{|n|>\delta} = H = \text{const.} \tag{9}$$

This implies that $U_p(s, n) = U(s, n)$ outside the wake, and inside the wake U_p is the velocity implied by the Bernoulli equation for irrotational flows. In other words U_p is an extension of the external potential-flow velocity into the wake. If (9) is used with (7) to eliminate p/ρ, we obtain

$$U_p^2 = 2H - 2\frac{p_0}{\rho} - \frac{2}{R}\int_0^n U^2\,\mathrm{d}n. \tag{10}$$

Since the curvature term in this equation is of a smaller order of magnitude than all the other terms, U^2 in the integral may be approximated by its representative value $U_{p0}^2 = U_0^2(s, 0)$. Then a first approximation to U_p may be given as a linear variation

$$U_p = U_{p0}\left(1-\frac{n}{R}\right), \tag{11}$$

where $U_{p0}(s) = U_p(s, 0) = [2(H-p_0/\rho)]^{\frac{1}{2}}$. This is the potential-flow velocity used by So & Mellor (1973) for analysing boundary-layer data on curved surfaces.

Based on U_p, as defined by (10), a defect velocity U_d can be defined by

$$U_d = U_p - U. \tag{12}$$

The x-component momentum equation can now be written in a form that is accurate to the order of $U_1 U_s/L$. Noting that $U_d \sim U_s$, the result becomes

$$U_p\frac{\partial U_d}{\partial s} + V\frac{\partial U_d}{\partial n} = -U_d\frac{\partial U_p}{\partial s} + V\frac{\partial U_p}{\partial n} + \frac{U_p V}{R} + \frac{\partial}{\partial n}\overline{uv}. \tag{13}$$

This is the transport equation for the defect velocity U_p. The equation can be linearized in terms of U_d since

$$V = -\int_0^n \frac{\partial U}{\partial s}\,\mathrm{d}n \approx -\int_0^n \frac{\partial U_p}{\partial s}\,\mathrm{d}n \tag{14}$$

by continuity, and we have assumed that $U_d \ll U_p$. In this case, (13) is a linear transport equation for the defect velocity U_d. The first term on the right-hand side represents the pressure gradient, while the second and third terms represent the curvature effects. If the linear approximation (11) is applicable, the curvature-related terms disappear, reducing the momentum equation to that for straight linear wakes, except for U_p which varies across the wake.

An alternative to introducing the defect velocity is to consider the mean vorticity $\Omega \equiv \partial V/\partial s - \partial/\partial n[(1+n/R)\,U]$, which, by the present order-of-magnitude assumptions, may be approximated by

$$\Omega = -\frac{U}{R} - \frac{\partial U}{\partial n}. \tag{15}$$

The transport equation for Ω reduces to

$$U\frac{\partial\Omega}{\partial s}+V\frac{\partial\Omega}{\partial n}=\frac{\partial^2}{\partial n^2}\overline{uv} \tag{16}$$

if only terms of highest order are retained. This equation is identical with that for thin boundary layers, and indicates that the effects of curvature (and pressure gradient) on the vorticity come through the shear stress only. The transport equations for the shear stress and other Reynolds stresses are given below.

The transport equations for $\overline{u^2}$, $\overline{v^2}$, $\overline{w^2}$, $\frac{1}{2}\overline{q^2}$ and $\overline{uv}$ will reduce to

$$U\frac{\partial}{\partial s}\overline{u^2}+V\frac{\partial}{\partial n}\overline{u^2}=-2\overline{uv}\frac{\partial U}{\partial n}-2\overline{u^2}\frac{\partial U}{\partial s}-2\overline{uv}\frac{U}{R}-\frac{\partial}{\partial n}(\overline{u^2v})+2\overline{\frac{p'}{\rho}\frac{\partial u}{\partial s}}-\epsilon_u, \tag{17}$$

$$U\frac{\partial}{\partial s}\overline{v^2}+V\frac{\partial}{\partial n}\overline{v^2}=2\overline{v^2}\frac{\partial U}{\partial s}+4\overline{uv}\frac{U}{R}-\frac{\partial}{\partial n}\left(\overline{v^3}+2\frac{\overline{vp'}}{\rho}\right)+2\overline{\frac{p'}{\rho}\frac{\partial v}{\partial n}}-\epsilon_v, \tag{18}$$

$$U\frac{\partial}{\partial s}\overline{w^2}+V\frac{\partial}{\partial n}\overline{w^2}=-\frac{\partial}{\partial n}(\overline{vw^2})+2\overline{\frac{p'}{\rho}\frac{\partial w}{\partial z}}-\epsilon_w, \tag{19}$$

$$U\frac{\partial}{\partial s}\overline{uv}+V\frac{\partial}{\partial n}\overline{uv}=-\overline{v^2}\frac{\partial U}{\partial n}+\overline{u^2}\frac{U}{R}-\frac{\partial}{\partial n}\left(\overline{uv^2}+\frac{\overline{up'}}{\rho}\right)+\overline{\frac{p'}{\rho}\frac{\partial v}{\partial s}}+\overline{\frac{p'}{\rho}\frac{\partial u}{\partial n}}, \tag{20}$$

$$U\frac{\partial}{\partial s}\tfrac{1}{2}\overline{q^2}+V\frac{\partial}{\partial n}\tfrac{1}{2}\overline{q^2}=-\overline{uv}\frac{\partial U}{\partial n}-(\overline{u^2}-\overline{v^2})\frac{\partial U}{\partial s}+\overline{uv}\frac{U}{R}-\frac{\partial}{\partial n}\left(\tfrac{1}{2}\overline{vq^2}+\frac{\overline{vp'}}{\rho}\right)-\epsilon, \tag{21}$$

where p' is the fluctuating pressure, ϵ_u, ϵ_v, ϵ_w and $\epsilon=\frac{1}{2}(\epsilon_u+\epsilon_v+\epsilon_w)$ are the rates of dissipation of $\overline{u^2}$, $\overline{v^2}$, $\overline{w^2}$ and $\frac{1}{2}\overline{q^2}\equiv\frac{1}{2}(\overline{u^2}+\overline{v^2}+\overline{w^2})$ respectively. These transport equations are the same as those for boundary layers on a mildly curved surface ($\delta\ll R$). The terms on the right-hand side of these transport equations are arranged in order of production (generation), diffusion, pressure redistribution and dissipation (destruction). Production terms are arranged in order of shear production, normal-stress production, and production due to curvature.

These equations have been studied by Bradshaw (1973) and others. The influence of the extra rate of strain comes through the extra production terms. The importance of these terms has been shown by Hunt & Joubert (1979), Gibson & Rodi (1981) and Shizawa & Honami (1983). Since the streamwise strain $\partial U/\partial s$ is very closely related to the pressure gradient the generation terms due to normal stresses are related to the pressure gradient. They tend to increase $\overline{u^2}$, decrease $\overline{v^2}$, and have no direct influence on $\overline{w^2}$ in the region where $\partial U/\partial s>0$. The opposite is true for $\partial U/\partial s<0$. The positive curvature $R>0$ tends to increase $\overline{u^2}$, decrease $\overline{v^2}$ and decrease $\overline{q^2}$ in the region of positive shear stress $-\overline{uv}$. The shear stress $-\overline{uv}$ tends to be increased in every case. Due to the importance of the relative magnitudes of turbulence production caused by pressure gradient and streamline curvature, the following ratios of these production terms are often used to quantify their importance:

$$F=\frac{(\overline{u^2}-\overline{v^2})\,\partial U/\partial s}{\overline{uv}\,\partial U/\partial n} \tag{22}$$

and

$$-S=\frac{\overline{uv}\,U/R}{-\overline{uv}\,\partial U/\partial n}=-\frac{U/R}{\partial U/\partial n}, \tag{23}$$

which are the ratios of the production of $\frac{1}{2}\overline{q^2}$ due to the normal stresses and the curvatures respectively, to the production due to the shear stress.

In the small-defect wake, both of these parameters can become of the order of

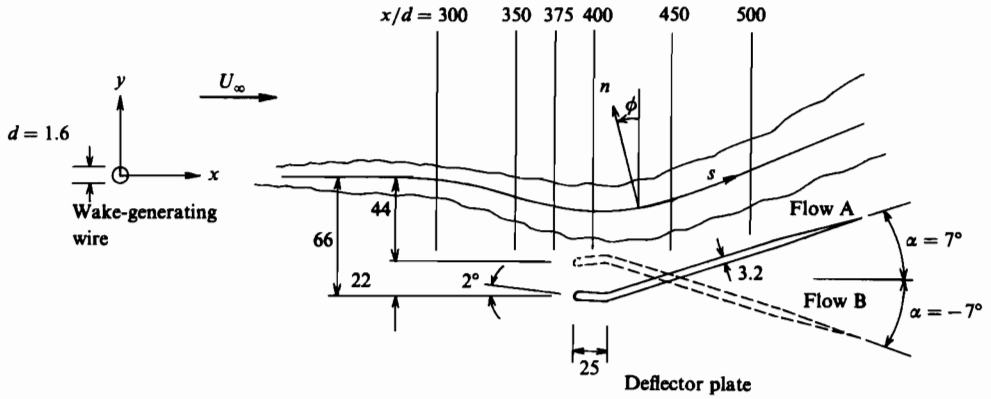

FIGURE 1. Arrangement of wake generator and deflector plate; dimensions are in mm.

unity. In boundary layers, in which these parameters are of the order of unity, the structure of the Reynolds stresses is known to be very different from those in plane flows at constant pressure. The values of S in the present experiments are in the range of other 'highly' curved shear flows. It is, therefore, expected that either the pressure gradient and curvature effects are very large, or the significance of the values of these parameters in small-defect wakes must be different from those in the other shear flows.

3. Experimental arrangements and measurement methods

The arrangement of the wake generator and the deflector plate is shown in figure 1. A wire of diameter 1.6 mm was used to generate a plane wake. The deflector plate was placed below the wake at two angles, $\pm 7.0°$, since only a mild deflection was needed. The deflector was a 254 mm long, 3.2 mm thick aluminium plate which had a 25 mm long leading-edge nose hinged on the main deflector. The purpose of the rotatable leading edge was to avoid the separation that can occur on the leeward side of the plate. With the leading edge inclined opposite to the direction of inclination of the main plate, the boundary layers could be maintained attached up to an angle of attack of about 10°. The flow when the angle of attack of the deflector is $+7°$ will be referred to as Flow A and that corresponding to $-7°$ will be called Flow B. The angle between the chord of the leading-edge device and the free-stream direction was set at $\pm 2.0°$ for Flows B and A respectively. The relative positions of the wake generator and the deflector plate were selected so that there would be a sufficiently large potential-flow region between the wake and the boundary layers on the plate, and such that a sufficient local curvature was obtained. The total turning angle of the wake is roughly independent of the relative positions, but the magnitude of the curvature changes. With the relative positions indicated in figure 1, the streamwise distance over which the wake was curved was approximately five wake thicknesses.

Measurements were made at the six streamwise stations indicated in figure 1. At each streamwise station, a TSI 1243 X-wire probe was traversed vertically (constant x) covering the entire wake proper and some external flow. The free-stream velocity U_∞ was kept constant within 1 % of 15 m/s, corresponding to a Reynolds number, based on wire diameter, of 1550. The hot wires were operated by two TSI 1050 constant-temperature anemometers. Output signals of the anemometers were filtered

between 5 Hz and 10 KHz, and recorded on $\frac{1}{4}$ in. magnetic tape using the f.m. channels of a B&K 7003 tape recorder. These signals were later transferred to another tape recorder (HP 3968A) at $\frac{1}{10}$th of the recording speed, and then the signals were further reproduced by the HP recorder at one quarter of its recording speed. The reproduced signals were sampled and digitized using a 12-bit analog-to-digital converter (Cyborg Isaac 91A) controlled by an Apple II microcomputer. The large speed reduction from the original recording was required to reduce the instantaneous velocity components, since the digitizer employed had a slow conversion rate of 1 KHz and employed non-simultaneous sampling. During the signal handling, the gains of the input and output amplifiers were carefully adjusted to minimize the signal distortion and the noise. The precise gain and the phase shift between the channels were determined by letting sine-wave calibration signals of known amplitude and frequency go through the entire system. The overall signal-to-noise ratio is estimated to be better than 50. At the reduced speed, the effective sampling rate is 20 kHz (equal to the Nyquist frequency corresponding to a low-pass-filter setting of 10 kHz) in real time. Only a few data points were sampled at this rate at one time, and they were used to correct for the delay between the two channels and to obtain temporal derivatives of the instantaneous velocities. This process was repeated 4000 times, spread over the time of 30 s, to obtain good convergence of the averages of velocities and products of fluctuating velocities and the time derivatives. More details of the data processing are given by Akdag *et al.* (1984). The present digital analysis that reduces all the moments and mixed moments of u and v up to fourth-order, and the second- and third-order moments of time derivatives, was made at selected stations only. At the rest of the stations (in fact at all measurement positions), real-time analog averaging was done to calculate mean-velocity components and Reynolds stresses, $\overline{u^2}$, $\overline{v^2}$ and $\overline{uv}$.

The probe was calibrated at a fixed point in the free stream upstream of the deflector plate. The probe calibration yielded the constants in the usual Kings-law response equation with exponent 0.45 and the angle in the cosine law. The calibrations were done immediately before and after each traverse by translating the probe to the fixed calibration position. Since the probe was moved to the calibration position by keeping the probe angle fixed, there was no probe misalignment. The flow directions were determined within the accuracy of the angle calibration, which was about 0.1°.

The usual problem of reducing statistics of derivatives is the spatial and temporal resolution of the probe. From the spectral data of Uberoi & Freymuth (1969), taken in a straight-cylinder wake at constant pressure (and also from the present results), the Kolmogoroff length η at the centre of the most upstream station, $x/d = 300$, where η is smallest, is estimated to be 0.2 mm. The corresponding frequency f in a flow of mean velocity $U \approx 15$ m/s is $f = U/(2\pi\eta) \approx 12$ KHz. The length of the hot wire was 0.7 mm and signals that are low-pass filtered at 10 KHz should represent the small-scale fluctuations adequately.

The two dimensionality of the flow was tested by a few spanwise traverses of the probe. The uniformity of the mean flow and the Reynolds stresses was confirmed within 0.5 % and 5 % respectively, over about 6 wake thicknesses in the centre portion of the tunnel.

4. Experimental results

In this section, basic results from the measurements are presented. As described in §3, the measurements were made in (x, y)-coordinates, but appropriate interpre-

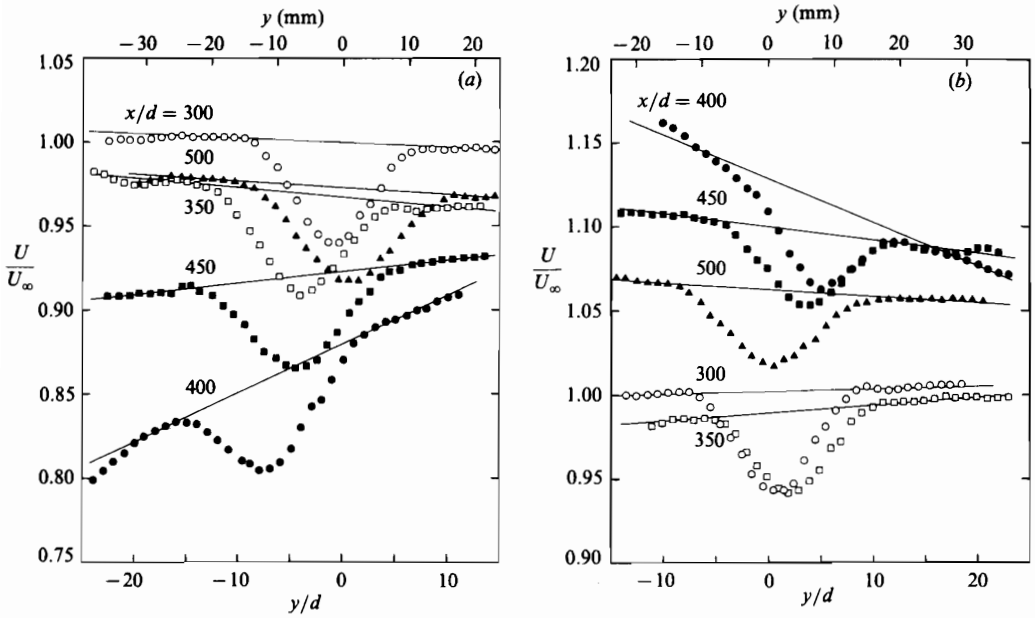

FIGURE 2. Mean-velocity profiles: (*a*) Flow A, (*b*) Flow B. ○, $x/d = 300$; □, 350; ●, 400; ■, 450; ▲, 500; ——, straight-line fit to velocity near and outside wake edges.

tations should be made in the (s, n)-coordinates used in §2. Since the inclination of the coordinate line, $n = 0$, is at the most $\pm 7°$, use of y, relative to $y_c(x)$, which is the vertical position where the defect velocity defined by (12) is maximum, is a reasonable approximation to n, and $x = \text{const.}$ corresponds to $s = \text{const.}$ with a similar small discrepancy. The s- and n-direction components of the velocities are easily deduced from those in the (x, y)-coordinates. The results presented here are for s- and n-direction components at points defined in (x, y)-coordinates.

It is preferable to present the data in similarity coordinates using s and n in place of x and y, so that the results can be directly compared with similar profiles of the self-preserving straight wakes. The lengthscale l_0 and the velocity scale u_0 of the self-preserving wake are $(d(x-x_0))^{\frac{1}{2}}$ and $U_\infty(d/(x-x_0))^{\frac{1}{2}}$, respectively. Here d is the diameter of the wake-generating cylinder and x_0 is the virtual origin of the wake. Therefore, most of the data are normalized by l_0 and u_0 and plotted against $(y-y_c)/l_0$. The value of x_0 used is $-40d$. This value was found by Fabris (1979) to allow the profiles of mean velocity, Reynolds stresses and triple products in the range of $x/d = 200$ to 400 to be nearly self-similar. However, it must be noted that Townsend (1949) used $x_0 = 90d$ to collapse his data, which were obtained further downstream where more rigorous self-preservation was confirmed.

4.1. *Mean-velocity data*

The distributions of the mean velocity in the two wake flows are shown in figure 2(*a*, *b*). The hypothetical potential-flow velocity U_p determined by fitting a straight line to the mean-velocity distribution near the wake edges is also shown. Determination of U_p using the definition (9) was not possible since the pressure was not directly measured. However, the present linear fit agreed very well with the approximation (11), and thus this U_p will be used for further data analysis.

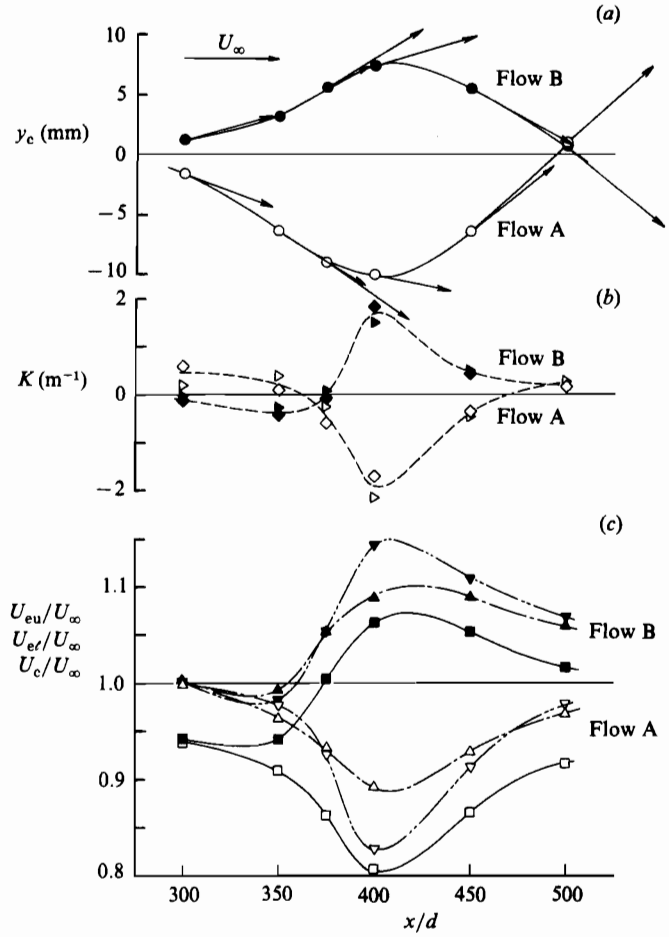

FIGURE 3. Trajectory and curvature of the wake centre and velocities at the centre and edges of the wake: open symbols, Flow A; filled symbols, Flow B; →, mean-velocity vector at $y = y_c$; ◇, ◆, K from double differentiation of y_c; ▷, ▶, K from straight-line fit to mean velocity outside wake and (11); △, ▲, U_{eu}/U_∞; ▽, ▼, $U_{e\ell}/U_\infty$; □, ■, U_c/U_∞.

At the first measurement station, $x/d = 300$, the velocity profiles in both flows are very close to symmetric so that it may be said that the effects of the curvature have not yet set in. Up to $x/d = 350$ the velocity decreases in both flows. At $x/d = 400$, the strongest asymmetry is seen. Downstream of this position the wakes start to recover symmetry. The most asymmetric profile of the present flows still contains the minimum-velocity point, and the degree of asymmetry is similar to that at the initial turning of Savill's (1983) curved wake.

The path of the wake, degree of the wake curvature and the pressure gradients are shown in figure 3. The trajectory $y = y_c$ and the mean velocity vector at this condition are shown in figure 3(*a*). It should be noted that the vertical distances are expanded by a factor of 10 relative to the horizontal distances. The mean-velocity vectors at $y = y_c$ are seen to be nearly tangent to the curve $y = y_c$ so that this curve may be regarded as a mean streamline as well as the wake centreline (being the position of maximum defect velocity). The wake paths in both flows are qualitatively similar

$\frac{x}{d}$	$\frac{U_{eu}}{U_\infty}$	$\frac{U_{e\ell}}{U_\infty}$	$\frac{U_c}{U_\infty}$	y_c (mm)	ϕ (deg)	K (m^{-1}) †	K (m^{-1}) ‡
			Flow A				
300	0.998	1.003	0.939	−1.6	−2.1	0.58	0.17
350	0.963	0.975	0.909	−6.3	−3.6	0.09	0.40
375	0.933	0.925	0.864	−9.0	−4.1	−0.60	−0.24
400	0.891	0.827	0.805	−10.0	−1.2	−1.70	−2.15
450	0.928	0.913	0.865	−6.4	4.7	−0.38	−0.46
500	0.968	0.977	0.916	1.0	5.0	0.15	0.28
			Flow B				
300	1.004	1.002	0.943	1.3	1.6	−0.16	−0.09
350	0.991	0.981	0.941	3.2	3.2	−0.46	−0.29
375	1.053	1.054	1.004	5.6	3.5	−0.08	0.03
400	1.089	1.144	1.063	7.4	1.7	1.84	1.47
450	1.089	1.106	1.053	5.5	−3.3	0.42	0.45
500	1.059	1.067	1.017	0.6	−4.7	0.14	0.22

† From double differentiation of y_c.
‡ From straight-line fit to mean velocity outside wake and (11).

TABLE 1. Mean-flow parameters

to the streamlines of the potential-flow solution near an inclined flat plate in a uniform stream. Upstream of the deflector plate they deflect in the opposite direction before starting to follow the direction tangent to the deflector plate. In the centre of the figure, the curvature of the streamline along the wake centre, calculated by two methods, is shown. The first method used is the graphical differentiation of the equation for the trajectory of the wake centre. The second method is based on the approximation represented by (11). According to this approximation, the slope of the linear fit to the potential-flow velocity U_p is $-U_{p0}/R$ and is related to the curvature $K = 1/R$. These slopes and U_{p0} were obtained from the fitted straight lines shown in figure 2(*a*, *b*), and K was calculated. It can be seen that the results of the two methods agree very well, indicating that the approximation (11) is valid and the linear fit to U_p, shown in figure 2(*a*, *b*), is very good. Note that in both flows, the largest curvature is only 2 m^{-1}, or the smallest radius of curvature is about 0.5 m, so that δ/R is about 0.025.

In figure 3(*c*), the minimum velocity U_c, and velocities U_{eu} and $U_{e\ell}$ at the upper and lower 'edges' of the wake respectively are shown. The edges are taken at $y = y_c \pm 5((x-x_0)\,d)^{\frac{1}{2}}$ which are the edges of the straight wake where x_0 is the virtual origin of the wake taken to be $-40d$ as described earlier. These edge velocity distributions indicate the magnitude of asymmetry relative to the wake depth. Also, the difference between U_{eu} and $U_{e\ell}$ indicate the magnitudes of the net pressure variation across the wake. In both cases, in the initial region up to $x/d = 350$, the wake is subjected to a small adverse pressure gradient as it shifts slightly in the direction opposite to the main deflection direction. In the region between $x/d = 350$ and 400, Flow A undergoes an adverse pressure gradient while Flow B is accelerated. At $x/d = 400$, the two wakes are deflected most strongly, and in the region downstream, both pressure gradient and curvature relax. The deceleration of Flow A prior to turning at $x/d \approx 400$ is milder than the acceleration of Flow B in the same region. The acceleration of Flow A after turning is stronger than the deceleration of Flow B in the corresponding region.

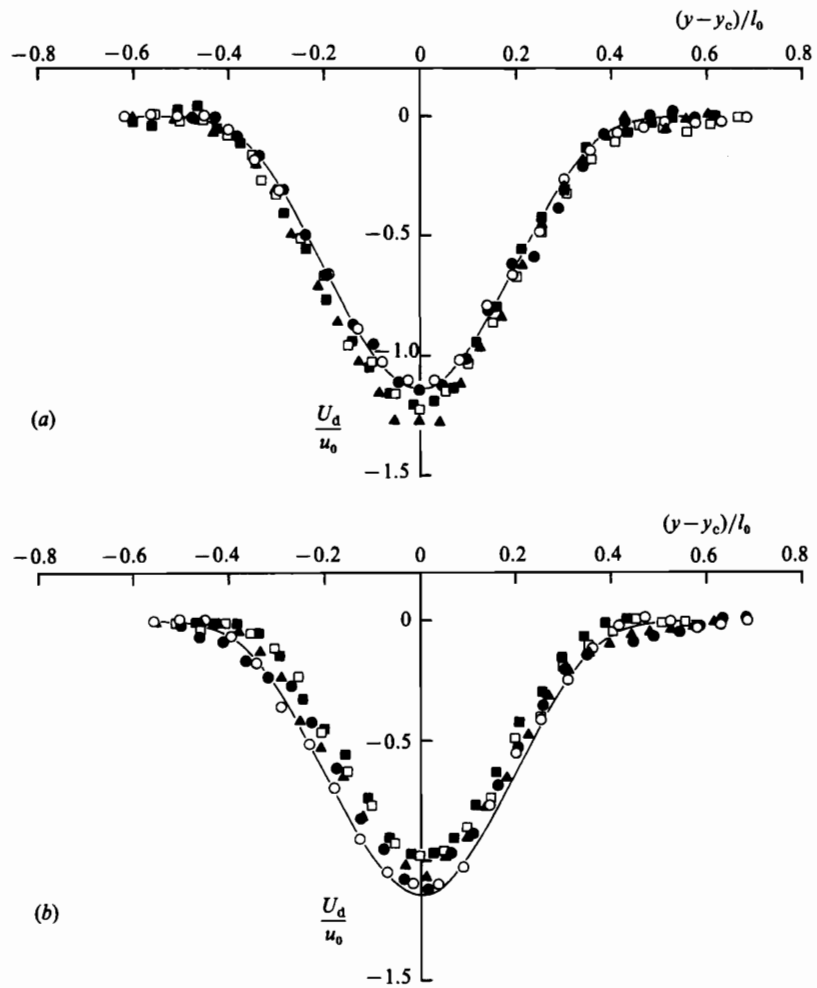

FIGURE 4. Mean defect-velocity profiles in similarity coordinates: (*a*) Flow A, (*b*) Flow B. ○, $x/d = 300$; □, 350; ●, 400; ■, 450; ▲, 500; ——, straight-wake data of Fabris (1979).

Although there are differences in the details of the pressure gradients and the curvature, Flows A and B are seen to be subjected to nearly opposite pressure gradients, and deflected in almost opposite directions. Some mean-flow parameters are listed in table 1.

Figure 4(*a*, *b*) displays the defect velocity $U_d(\equiv U_p - U)$ profiles) in similarity coordinates, i.e. the velocity is normalized by $u_0 = U_\infty(d/(x-x_0))^{\frac{1}{2}}$ and the transverse distance is normalized by $l_0 = (d(x-x_0))^{\frac{1}{2}}$. For comparison, Fabris' (1979) data, taken at $x/d = 400$ in straight wake, are shown as solid lines. The general growth in width and depth of the wake in Flow A and the shrinking and shallowing in Flow B are in agreement with the effects of pressure gradient seen by Hill *et al.* (1963). It appears that the wakes are slightly wider on the 'outer' side as they turn; otherwise there is no apparent asymmetric feature. Hence it may be said that the curvature effects on these defect-velocity profiles are small.

Figure 5(*a*, *b*) illustrates the profiles of the mean-velocity component V in the n direction. V in the present flows is very large, and is of the same order of magnitude

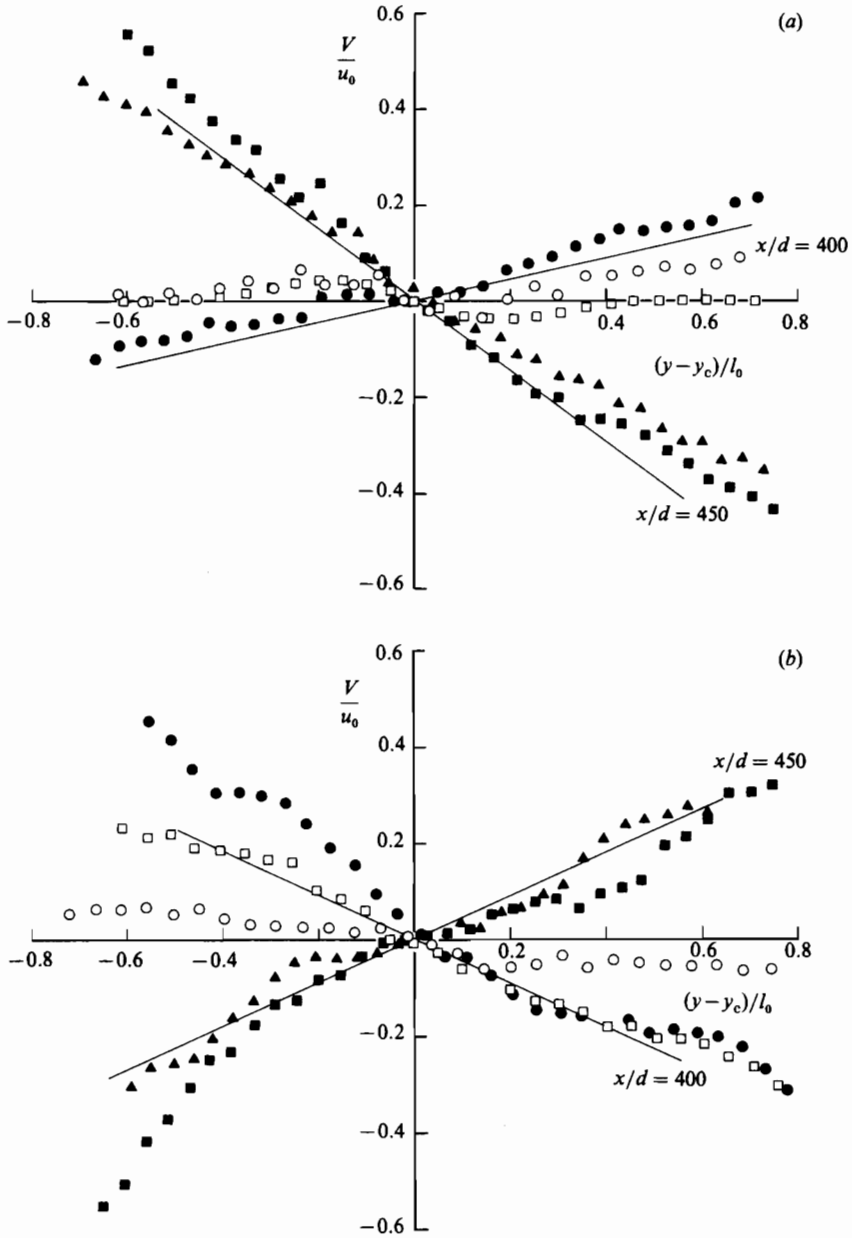

FIGURE 5. Mean normal velocity profiles in similarity coordinates: (*a*) Flow A, (*b*) Flow B. Symbols are as in figure 4; ——, $V = -(\mathrm{d}U_{\mathrm{p0}}/\mathrm{d}s)(y-y_{\mathrm{c}})$.

as the defect velocity U_{d}. The V-profiles of Flow A are nearly linear in n. The slope is related to $\partial U/\partial s$ by the continuity equation. The straight lines shown in figure 5 are

$$V = -\frac{\mathrm{d}U_{\mathrm{p0}}}{\mathrm{d}s}(y-y_{\mathrm{c}})$$

at $x/d = 400$ and 450. These straight lines approximate the actual V-distributions

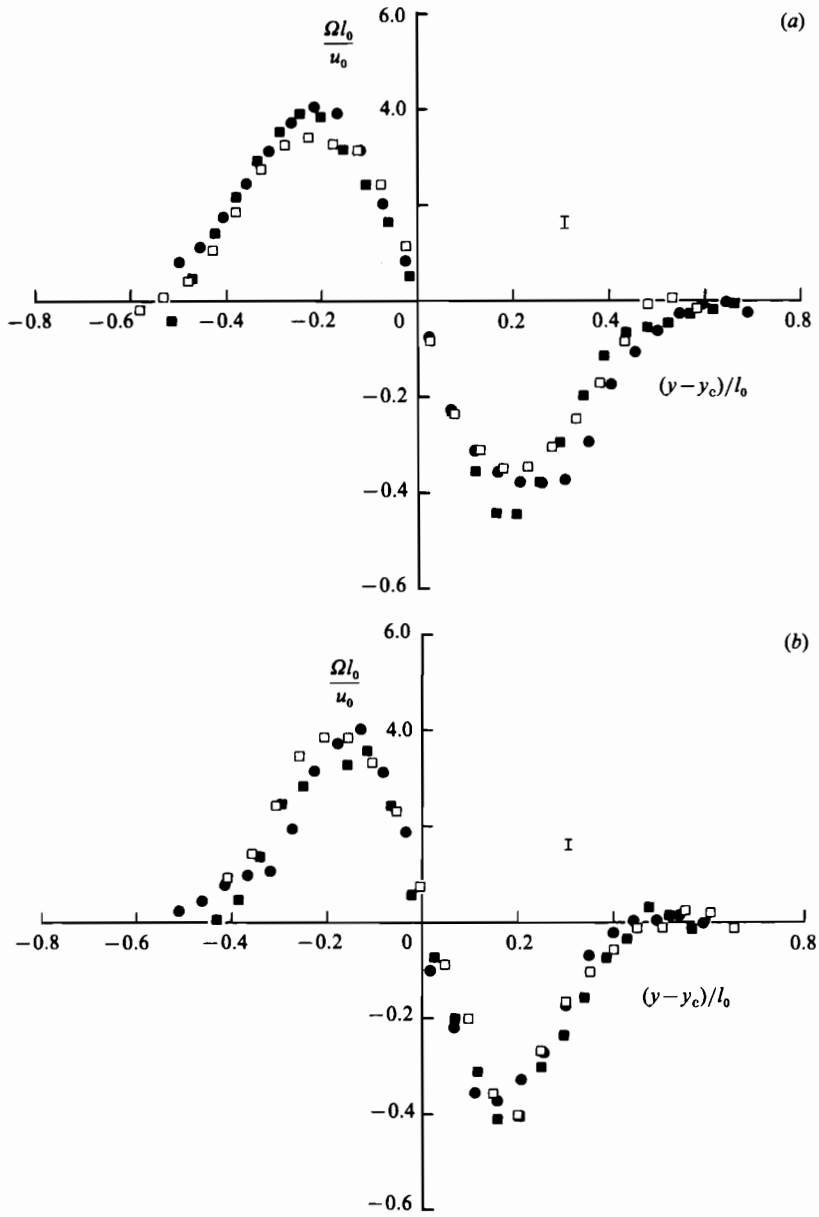

FIGURE 6. Mean-vorticity profiles: (*a*) Flow A, (*b*) Flow B. Symbols are as in figure 4; I, estimated magnitude of measurement and differentiation errors.

fairly well, although there is some discrepancy at $x/d = 400$ on the lower side of Flow B.

Mean-vorticity profiles are presented in figure 6(*a*, *b*), again in terms of the similarity coordinates. The reduction of Ω from the mean-velocity profiles involves graphical differentiation and is not very accurate. However, the results indicate, within the degree of uncertainty indicated by the estimated error bar, that the mean vorticity is not greatly influenced by the wake deflection. This indicates that the distortions in the mean-velocity profiles are mostly irrotational.

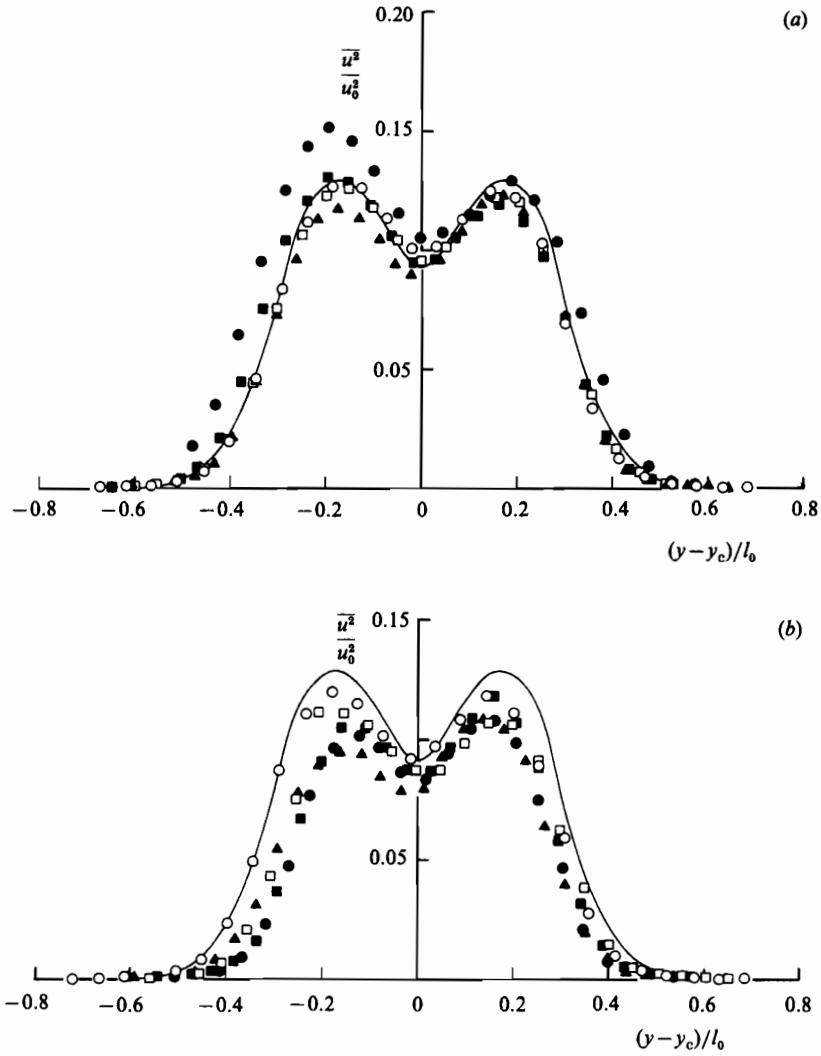

FIGURE 7. Streamwise fluctuations $\overline{u^2}$: (*a*) Flow A, (*b*) Flow B. ○, $x/d = 300$; □, 350; ●, 400; ■, 450; ▲, 500; ——, straight-wake data of Fabris (1979).

4.2. *Reynolds stresses*

Results of the Reynolds-stress components $\overline{u^2}$, $\overline{v^2}$ and $\overline{uv}$ are shown in figures 7–9. Again, they are presented in the similarity coordinates so that they may be compared with those obtained from an unperturbed straight wake. The data of Fabris (1979) are shown as solid lines for comparison purposes. Fabris' data were chosen for this comparison since his data were obtained at $x/d = 400$, which is in the middle of the present measurement region. Agreement between the present data at the most upstream station, $x/d = 300$, and the Fabris straight-wake data are good considering that the facilities and methods of measurement are quite different. The present $\overline{v^2}$ and the absolute values of $\overline{uv}$, however, are seen to be smaller. The shear correlation coefficient $-\overline{uv}/u'v'$, where $u' = \overline{u^2}^{\frac{1}{2}}$ and $v' = \overline{v^2}^{\frac{1}{2}}$, is also slightly smaller. In the present measurements, the wake-generating wire was only about 50 mm downstream

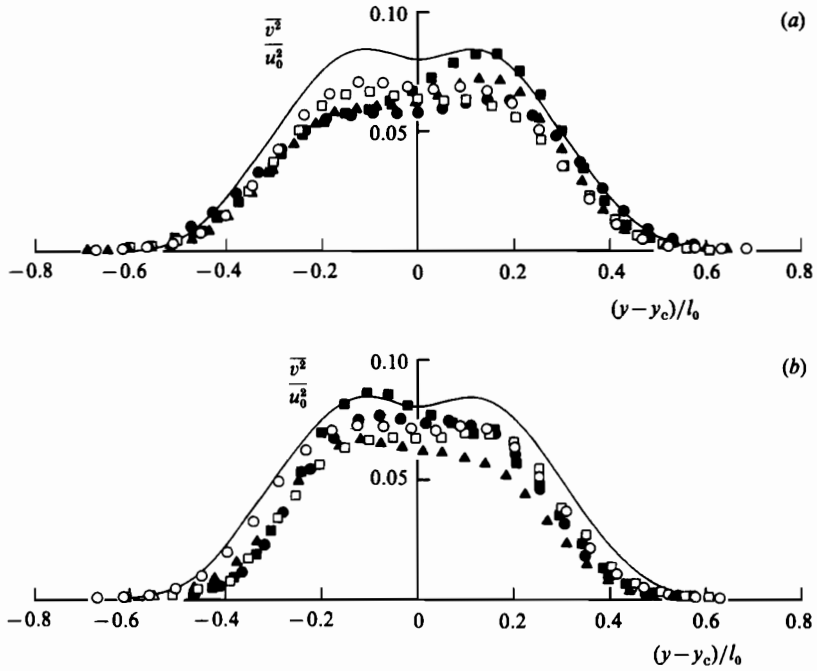

FIGURE 8. Transverse fluctuations $\overline{v^2}$: (*a*) Flow A, (*b*) Flow B. Symbols are as in figure 7.

of the wind-tunnel contraction, and the cylinder Reynolds number is about one half of Fabris', so that x_0 may have been slightly different from $-40d$. Also, the plot of U_{eu} and $U_{e\ell}$ shown in figure 3 indicates that there is a small adverse pressure gradient upstream of $x/d = 300$. This could be another reason for the lower $\overline{v^2}$ and lower $|\overline{uv}|$. Such trends in adverse pressure gradients were observed by Gartshore (1967). For the purpose of the present study, where the relative trends are most important, these small discrepancies are not serious if the present data at $x/d = 300$ are taken as the baseline straight-wake data.

At stations downstream of $x/d = 350$, a considerable amount of asymmetry, as well as across-the-wake trends, can be observed in all stress components. The strongest asymmetry is seen in the shear-stress profile at $x/d = 450$ of Flow A, and the streamwise intensity $\overline{u^2}$ of Flow B shows the least asymmetry.

The changes in the Reynolds-stress components $\overline{u^2}$, $\overline{v^2}$ and $\overline{uv}$ are much larger than would be expected to result from simple coordinate rotation. The change in $\overline{uv}$, caused by rotating the axes by an angle θ, for example, is $-(\overline{u^2}-\overline{v^2})\sin\theta\cos\theta$ (Castro & Bradshaw 1976) when θ is small, and is, at the most, about $0.005u_0^2$ in the present flows. The magnitudes and the sense of changes are largely as expected from the initial part of Savill's (1983) curved wake.

It is seen that the across-the-wake trends of Flow A and Flow B are actually opposite, which may be attributed to the opposite pressure gradients. The levels of $\overline{u^2}$ are generally higher in Flow A, and lower in Flow B, than the baseline levels at $x/d = 300$. The width of the wake, as implied by the region of non-negligible turbulence intensity, is wider in Flow A and narrower in Flow B. These trends are in agreement with the data of Gartshore (1967) and Narasimha & Prabhu (1972) that were obtained in wakes with pressure gradients. It is also seen that, although there is a considerable difference in the degree of asymmetry, the asymmetric features are

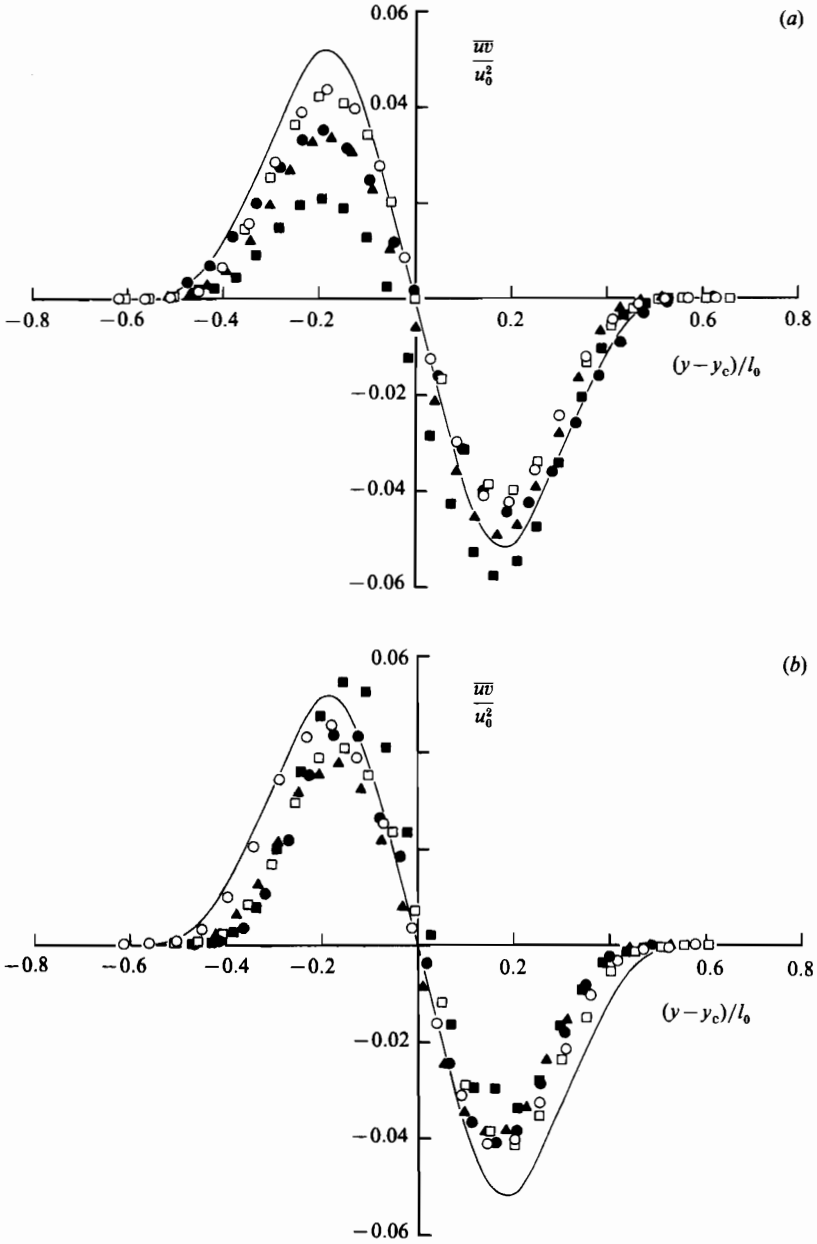

FIGURE 9. Reynolds shear stress $\overline{uv}$: (*a*) Flow A, (*b*) Flow B. Symbols are as in figure 7.

opposite for Flow A and Flow B, which are turning in opposite directions. Except for $\overline{u^2}$ in Flow A, the strongest asymmetric features are seen at station $x/d = 450$. It should be noted that the strongest asymmetry in the mean-velocity profiles was observed at the more upstream station, $x/d = 400$.

The value of $\overline{u^2}$ is larger on the lower half in Flow A, and on the upper half in Flow B and vice versa with $\overline{v^2}$. It is noted that the stability conditions imply increased turbulence on the upper side of Flow A and vice versa in Flow B. The increase of $\overline{u^2}$ on the stable side of the wake does not agree with the trend observed by Koyama

(1983) in the near wake ($x/d < 100$) nor with the results of Savill (1983), which show that $\overline{u^2}$ stays symmetric even after the wake has turned as much as 26°. However, the present trends do agree with the implications of the changes in the generation terms in the transport equations.

The Reynolds shear stresses shown in figure 9 (a, b) present the largest asymmetric features, indicating the strongest sensitivity to curvature. The large reduction in $\overline{uv}$ on the stable side of Flow A is in agreement with the results at the early stages of Savill's (1983) wake. It reduces to less than half at $x/d = 450$, compared with the initial station $x/d = 300$. It should be remembered that the ordinates are in similarity coordinates, so that the normal reduction in self-preserving situations does not show up in these plots. A decrease on the stable side of Flow B, and an increase on the unstable sides of both flows, are also seen at the same streamwise station, $x/d = 450$.

The development of the Reynolds-stress profiles also shows the dependence of curvature effects on the history of pressure gradients, or the interdependence between two effects. In Flow A, which is initially decelerated, asymmetry is obtained quickly and symmetry is recovered quickly as well. In Flow B, which is initially accelerated, the degree of asymmetry is smaller; it appears slowly and persists longer in the downstream adverse-pressure-gradient region ($x/d > 400$). At the most downstream station, $x/d = 500$, it still shows definite asymmetry. It appears that the curvature effects on $\overline{u^2}$ show up more easily and are maintained longer in an adverse-pressure-gradient environment.

4.3. *Averages of triple products*

For Reynolds-stress transport-equation modelling, the turbulent transport terms must be modelled, and experimental data are needed to guide this. Three such quantities, $\overline{u^2v}$, $\overline{v^3}$ and $\overline{uv^2}$, that are respectively the transports of $\overline{u^2}$, $\overline{v^2}$ and $\overline{uv}$, are shown in figure 10 (a–c) for Flow A. Reference is also made to the straight-wake data of Fabris (1983). The present data for $\overline{u^2v}$ and $\overline{uv^2}$ at $x/d = 350$ agree reasonably well with Fabris' data, while $\overline{v^3}$ is considerably smaller, probably for the same reason that the low $\overline{v^2}$ was seen earlier.

A significant feature of all these transport quantities is that they show more pronounced asymmetric features than changes in overall level, and the appearance of asymmetry is much more delayed than in the case of the Reynolds stresses. The Reynolds stresses all showed recovery, though not complete, at $x/d = 500$, but the triple products show strongest asymmetry at this most downstream location. They all show considerable increases on the unstable side and reductions on the stable side. This implies that considerable transport of Reynolds stress from the unstable side to the stable side continues after the turning is completed.

4.4. *Some detailed statistics of streamwise fluctuations*

Some results from further statistical analysis of the fluctuations of the streamwise velocity component are considered next. First, the skewness and the flatness factors of the fluctuating velocity component u as defined by

$$\frac{\overline{u^3}}{(\overline{u^2})^{\frac{3}{2}}}, \quad \frac{\overline{u^4}}{(\overline{u^2})^2}$$

are shown in figure 11 (a, b) for Flow A. The straight-wake data of Fabris (1983) are represented by a solid line. These quantities provide information on the shape of the probability-density function of u, and certain aspects of the turbulence structure.

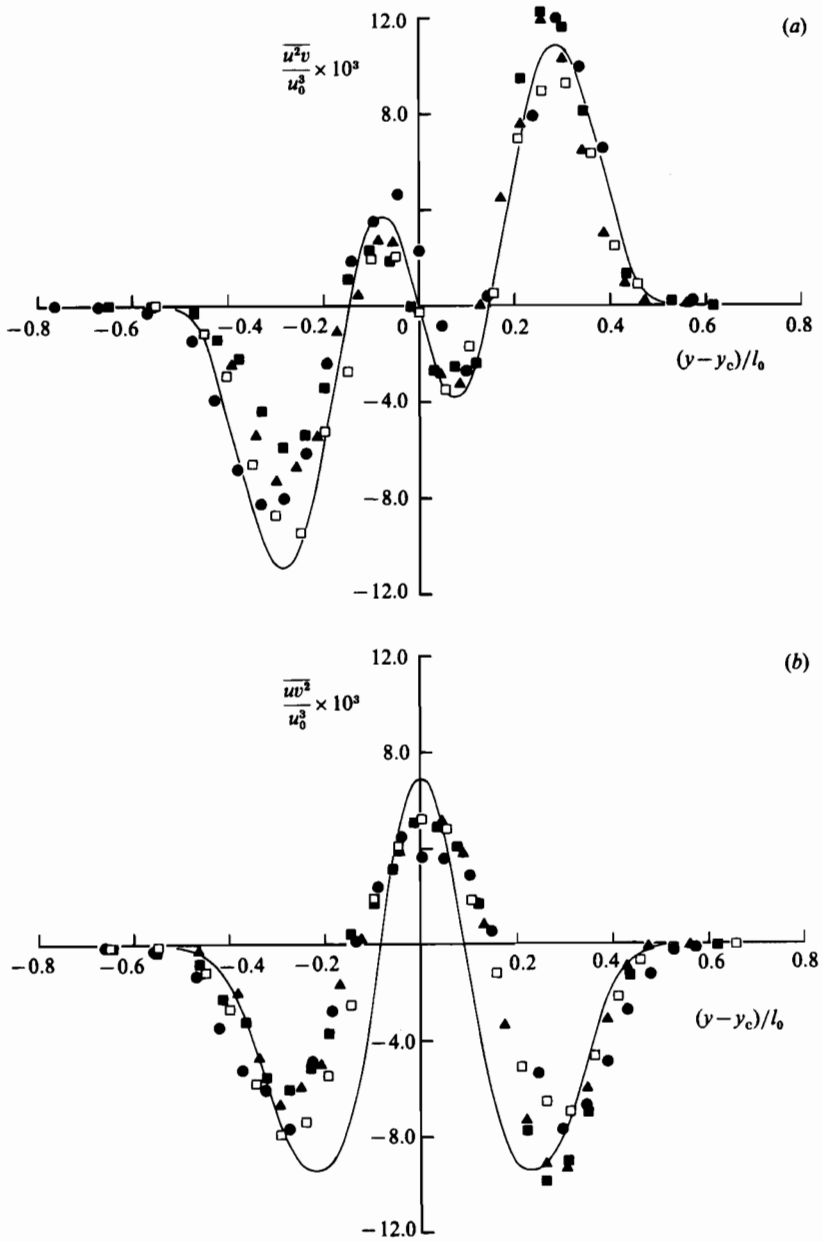

FIGURE 10 (*a*, *b*). For caption see facing page.

These results illustrate that the skewness and flatness factors in the present wake are not very much influenced by either the pressure gradient or the curvature. The distributions of the flatness factor, in particular, at all stations studied are very similar and agree well with the straight-wake data. If there is a close relationship between the flatness factor and the intermittency factor, as suggested by Townsend (1976), the present results indicate that the intermittency, which was not measured directly, is not influenced by the wake deflection. A close examination of figure 11 (*a*) reveals that the skewness factor is increased at $x/d = 400$, and appears to remain high

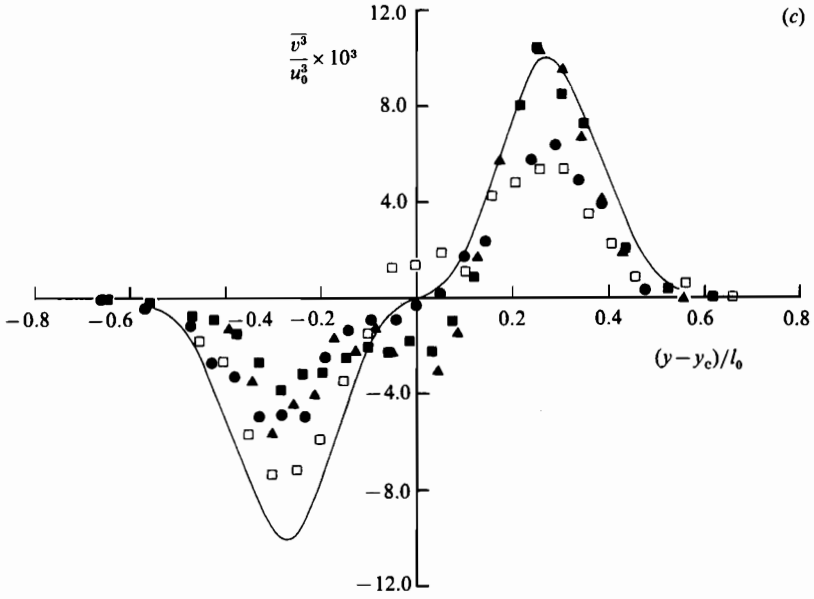

FIGURE 10. Averages of triple products in Flow A: (*a*) $\overline{u^2v}$, (*b*) $\overline{uv^2}$, (*c*) $\overline{v^3}$. Symbols are as in figure 7.

in the central region of the wake. More positive skewness implies the existence of sharper positive spikes in the u-signal.

Figure 12 presents the Taylor microscale λ defined by

$$\lambda^2 \equiv \overline{u^2}\overline{\left(\frac{\partial u}{\partial s}\right)^2},$$

where $\overline{(\partial u/\partial s)^2}$ is computed from $\overline{(\partial u/\partial t)^2}/U^2$, based on Taylor's frozen-turbulence assumption. It is seen that λ-distributions at all stations between $x/d = 350$ and 500 are quite symmetrical and stay fairly constant across the wake, showing the insensitivity of this quantity to the wake turning. The independence of the microscale from streamline curvature was also noted by Ramaprian & Shivaprasad (1978) in the case of mildly curving boundary layers. It is unfortunate that this lengthscale is not very useful for modelling the Reynolds stresses.

5. Discussion

5.1. *Effects of pressure gradient and streamline curvature*

The main purpose of the present investigation of two wakes is to study the effects of short regions of 'mild' pressure gradient and 'mild' curvature. The term 'mild' has been used since the lengthscale associated with the pressure gradient $U_{p0}/(dU_{p0}/dx)$ is much larger than the wake width δ, and the radius of the streamline curvature is also much larger than δ. The minimum values of the ratios of these quantities are $U_{p0}/(dU_{p0}/dx)/\delta = 25$ and $R/\delta = 25$. Indeed, the mean-velocity characteristics represented by the defect velocity relative to an appropriately determined potential-flow velocity in appropriately chosen curvilinear coordinates, were seen to be influenced very little by these effects and support the use of the term 'mild'.

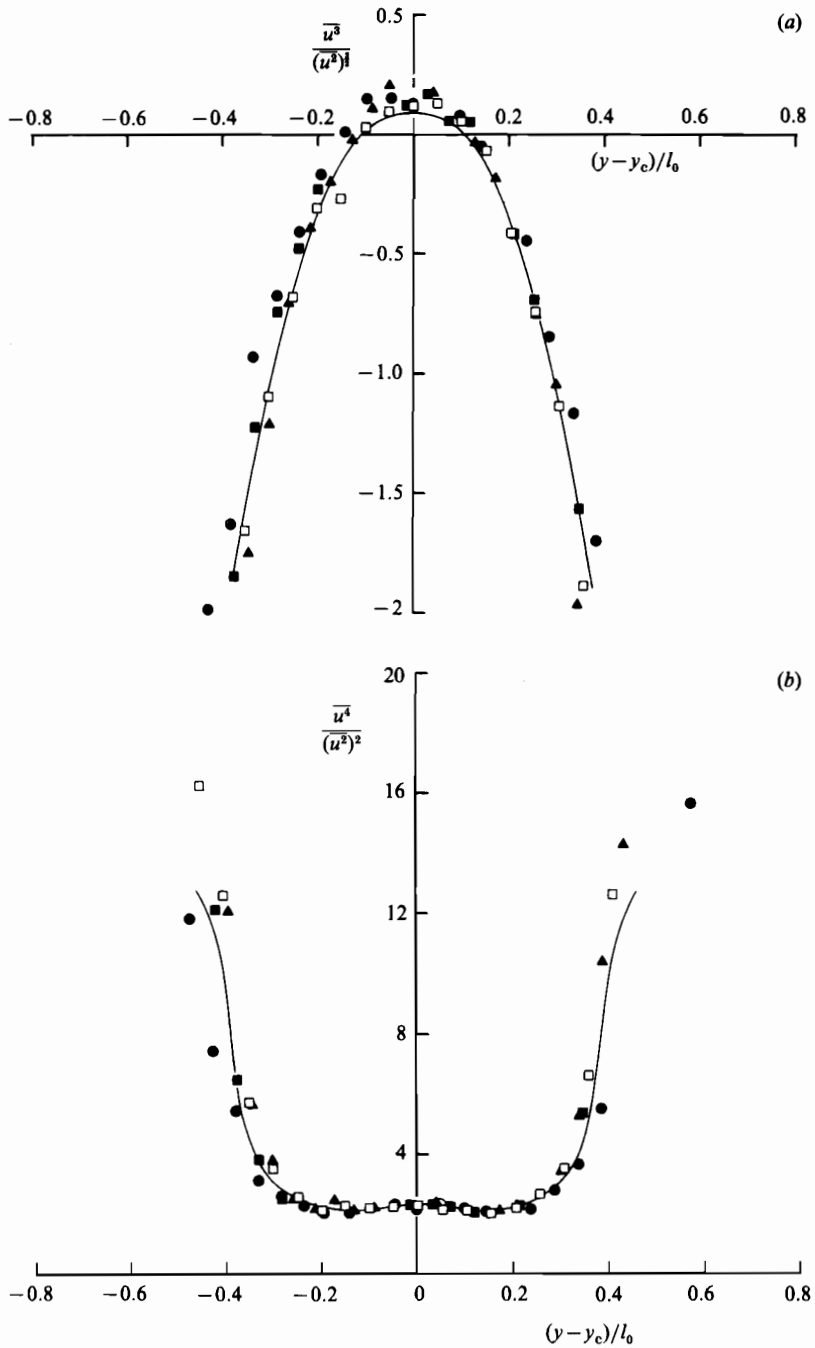

FIGURE 11. Skewness and flatness factors of streamwise fluctuations in Flow A: (*a*) skewness factor, (*b*) flatness factor. Symbols are as in figure 7; ——, straight-wake data of Fabris (1983).

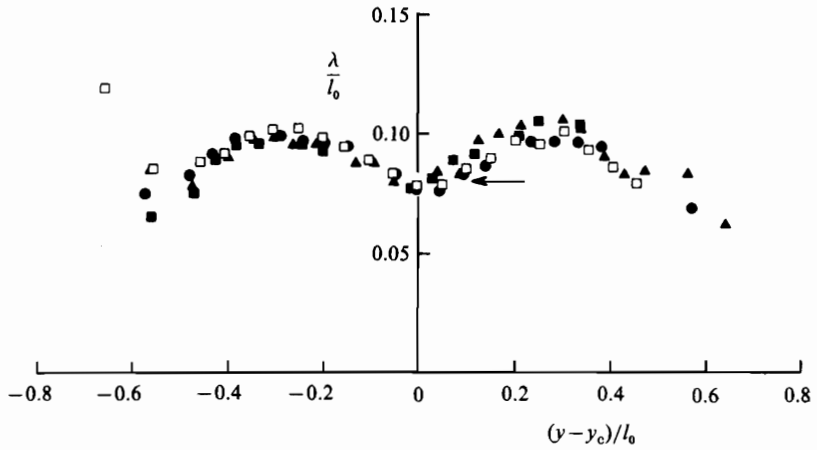

FIGURE 12. Taylor microscale λ in Flow A; symbols are as in figure 7; ←, data of Uberoi & Freymuth (1969) at the centreline.

Bradshaw (1973, 1975) classified shear layers according to the relative magnitudes of extra strain rate and simple shear strain $\partial U/\partial y$. A shear layer with an extra strain rate e, which may not satisfy $e(\partial U/\partial y)^{-1} \ll 1$ (the requirement for the thin-shear-layer or the boundary-layer approximations), but satisfies a more relaxed requirement, $e(\partial U/\partial y)^{-1} < 0.1$, is classified as a fairly thin shear layer. Bradshaw pointed out that, for fairly thin shear layers, the equations can be implemented by approximating some of the terms ignored in thin-shear-layer approximations, but the changes in turbulence structure may be significantly large. The analysis presented in §2 shows that the present wake flows do not satisfy the thin-shear-layer requirements. The measured data indicate that $|(\partial U/\partial x)(\partial U/\partial y)^{-1}|$ along the line of maximum $|\partial U/\partial y|$ is as large as 0.2 at $x/d \approx 350$ and 450, just before and after the turn. Also $|(\partial V/\partial x)(\partial U/\partial y)^{-1}|$ along the maximum $|\partial U/\partial y|$ exceeds 0.1 at stations between $x/d = 350$ and 450. The maximum value is reached at $x/d = 400$ on the stable side where $(\partial V/\partial x)(\partial U/\partial y)^{-1} \approx -0.5$ so that in terms of the ratio of the extra strain rate to the shear strain, the present wake flow violates even the requirements for the fairly thin shear layer. It is remarkable that this is the case even for a small turning of $\pm 7°$ over a few wake thicknesses. This may be compared with the strongly curved mixing layer of Castro & Bradshaw (1976), which turns as much as 90° over approximately 15 mixing-layer thicknesses and still satisfies the thin-shear-layer requirements for most of the regions.

Appropriate parameters of pressure gradients and curvature effects are F and S, as defined in (22) and (23). An indication of the magnitude of these parameters can be obtained from the plots of F and S at representative positions (maximum and minimum $\overline{uv}$ locations) in the upper and lower halves of the wake as shown in figure 13. The magnitudes of F and S are seen to be locally large, exceeding 0.4 at their peaks, but S at all other stations is smaller than 0.4.

It also can be seen in figure 13 that the curvature effects in Flow A and Flow B may not appear quite as opposite as indicated by the mean-flow parameters illustrated in figure 3. They are much larger in Flow A, which is subjected to an adverse pressure gradient first, than they are in Flow B. Also, they do not appear symmetrically. The absolute value of F in the lower half, for example, is much larger than that in the upper half. This makes the separation of the pressure-gradient effects

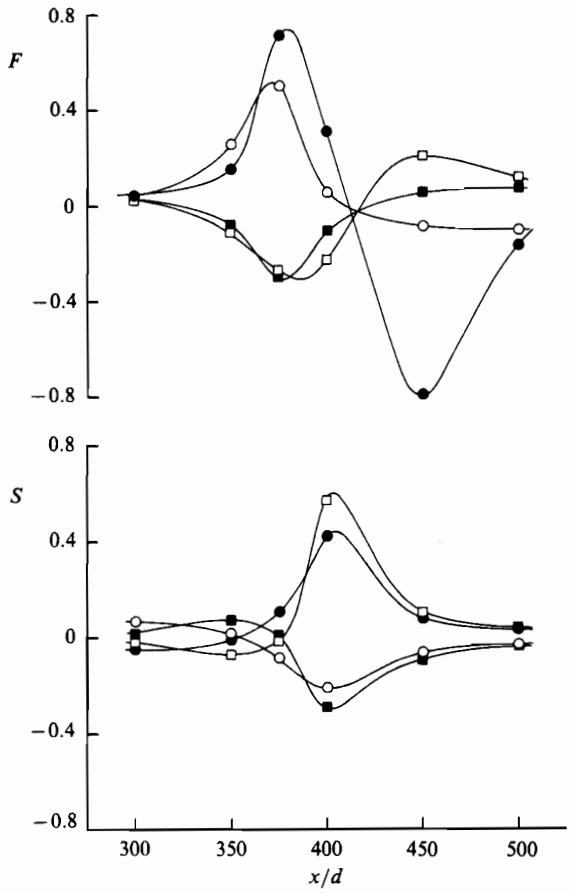

FIGURE 13. Pressure gradient parameter F and curvature parameter S; open symbols, maximum shear location in upper-half wake; filled symbols, maximum shear location in lower-half wake; circles, Flow A; squares, Flow B.

and streamline-curvature effects a little more difficult than originally desired. The distribution of S in Flow B, however, is very close to the mirror image of that in Flow A, and it can be expected that curvature effects will appear in Flow A and Flow B in opposite manners.

The overall effects on turbulence may be demonstrated by the changes in kinetic energy and shear stress. In figure 14 the maximum values of $\overline{u^2}+\overline{v^2}$, which are considered to represent the characteristics of the turbulent kinetic energy, and the maximum values of $|\overline{uv}|$, are plotted against streamwise distance. Since they are normalized by appropriate velocity scales of self-preserving straight wake, changes with respect to x may be regarded as the influence of the pressure gradient or the streamline curvature. It is seen that $\overline{u^2}+\overline{v^2}$ correlates better with the way F changes. In Flow B, in particular, the levels on the two sides are very close, and do not reflect the asymmetric feature implied by S. In fact, it will be seen that $\overline{u^2}+\overline{v^2}$ is very closely related to the total production. On the other hand $\overline{uv}$ is seen to be a very strong function of the curvature parameter S, although there is an apparent phase lag of approximately $50d$, which is approximately three wake widths. It is also noted that the fractional changes of $\overline{uv}$ are much larger than those of $\overline{u^2}+\overline{v^2}$, so that their ratio,

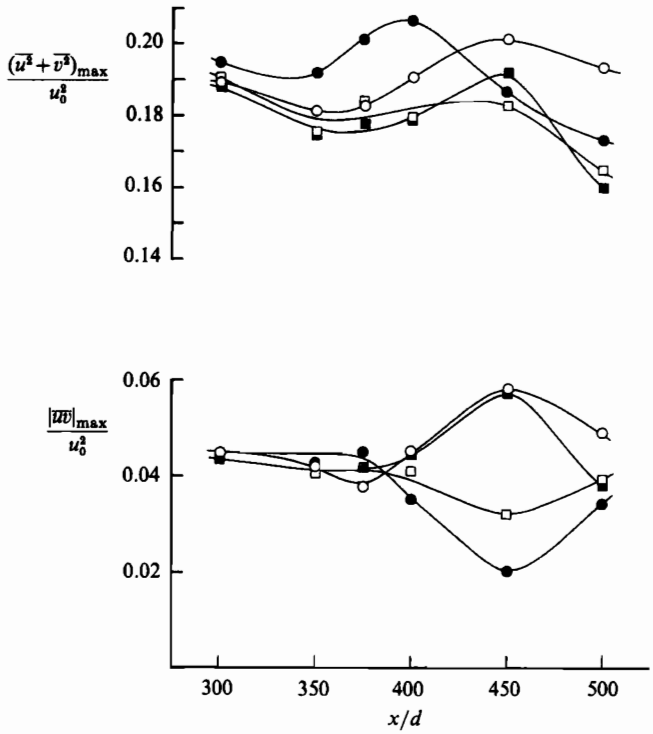

FIGURE 14. Streamwise variation of maximum values of $\overline{u^2}+\overline{v^2}$ and $|\overline{uv}|$; open symbols, upper-half wake; filled symbols, lower-half wake; circles, Flow A; squares, Flow B.

which resembles very closely the ratio of the shear stress to the turbulent kinetic energy, is a strong (but lagging) function of S. The lagged response in other curved flows has been previously demonstrated by Castro & Bradshaw (1976) and Smits *et al.* (1979).

5.2. *Turbulent-energy balance*

In this section, the terms in the transport equation (21) for the turbulent kinetic energy are examined. Calculated values for Flow A are shown in figure 15(*a–d*). Some assumptions have been made regarding averages involving the spanwise component of fluctuating velocity w, which was not measured. They are $\overline{w^2} = \frac{1}{2}(\overline{u^2}+\overline{v^2})$, and $\overline{w^2 v} = \frac{1}{2}(\overline{u^2 v}+\overline{v^3})$. The first of these was found to be satisfied approximately for much of the stable side of Savill's (1983) wake. The local-isotropy and frozen-turbulence assumptions are made to calculate the rate of dissipation of the turbulent kinetic energy $\epsilon = 15\nu(\partial u/\partial t)^2/U^2$. The diffusion due to the pressure fluctuations could not be obtained. If all the other terms were determined accurately, the pressure-diffusion terms could be obtained from difference, but the present data are not accurate enough to allow this. Hence, what is referred to as diffusion here is the diffusion or transport by fluctuating velocity.

The energy balance at $x/d = 350$ (figure 15*a*) is seen to be reasonably close to the straight-wake data of Townsend (1976), except that the production may be slightly smaller owing to the adverse pressure gradient in this region. At $x/d = 400$, the production increases drastically on the unstable side (upper half) and decreases on the stable side (lower half). It is observed to be negative near the lower edge. An

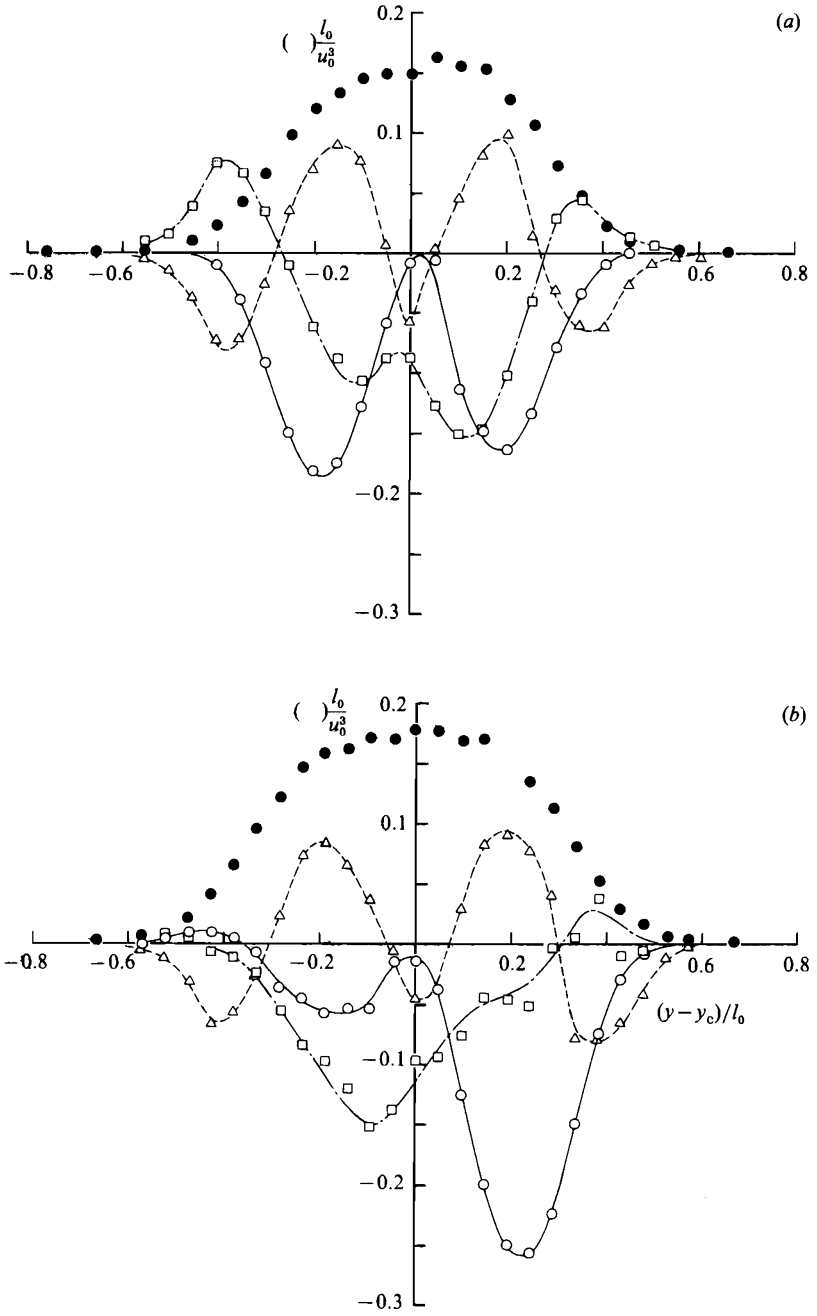

FIGURE 15(*a*, *b*). For caption see facing page.

examination of the production terms indicates that this negative production is caused by the extra (negative) production due to the curvature, and the production due to the shear stress stays positive throughout. This positive shear production was noted by Savill (1983) throughout his strongly curved wake. The diffusion appears to remain unchanged. The dissipation increases slightly throughout the wake, but does not show any decrease on the unstable side. Changes in the production are mostly balanced

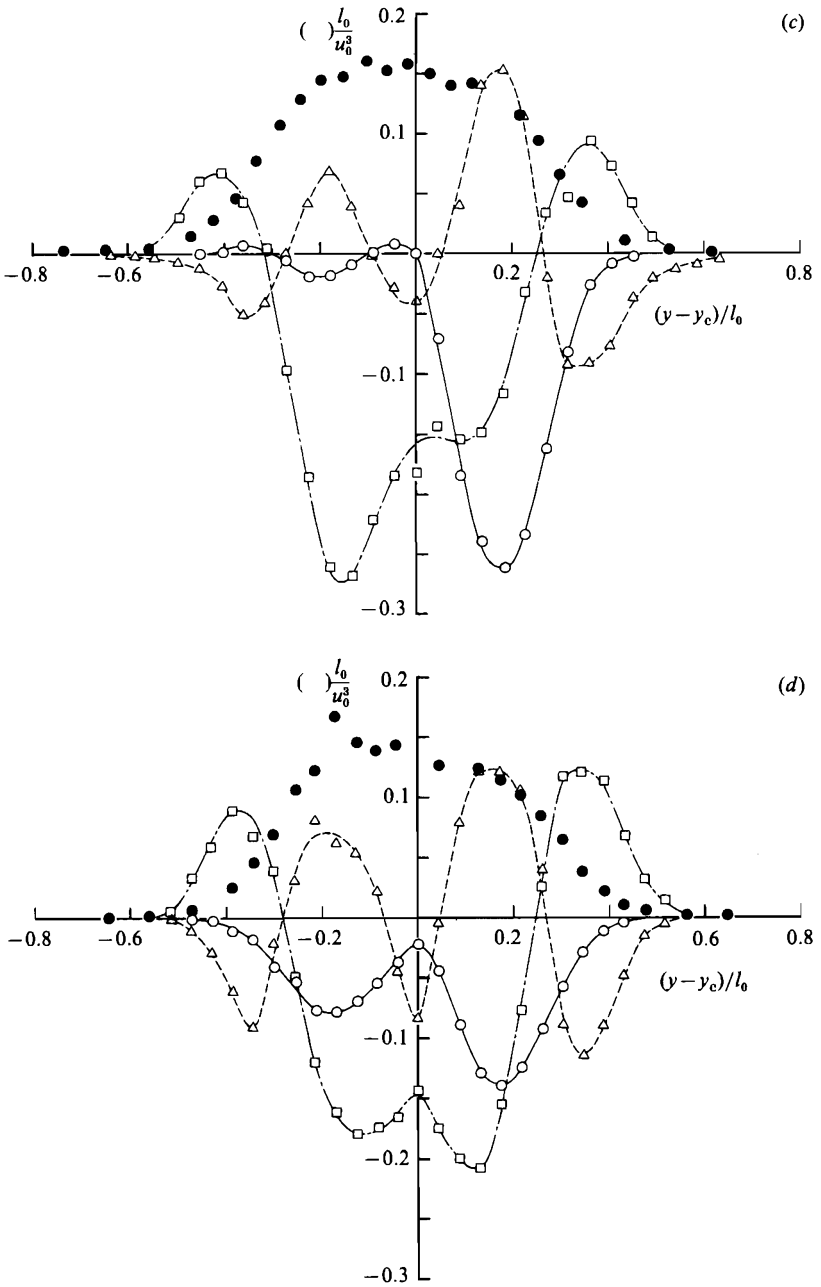

FIGURE 15. Turbulent-energy balance in Flow A: (*a*) $x/d = 350$, (*b*) 400, (*c*) 450, (*d*) 500. □, advection $U(\partial/\partial s)(\frac{1}{2}\overline{q^2}) + V(\partial/\partial n)(\frac{1}{2}\overline{q^2})$; ○, production $\overline{uv}(\partial u/\partial n) + (\overline{u^2} - \overline{v^2})(\partial U/\partial s) - \overline{uv}(U/R)$; △, diffusion $(\partial/\partial n)(\frac{1}{2}\overline{vq^2})$; ●, dissipation ϵ.

by the changes in the advection. This implies that the level of the turbulent energy change is directly due to the increased or reduced production.

At the next station, $x/d = 450$, the production terms continue to show a strong asymmetry. On the lower half it is almost zero, and even negative near the centre and the lower edge, which implies that the stabilizing effects come from the collapse

of the energy production. Unlike at $x/d = 400$, the main cause of the negative and low production is the (negative) normal-stress production. The extra production due to the curvature has dropped to an insignificant level. Production due to shear stress still remains positive throughout, and the large production on the other side is mostly due to this shear production. At this station the diffusion terms start to counterbalance part of the asymmetry in production terms, while the dissipation still appears to be uninfluenced. Here, the turbulent energy does not change as much as the production terms indicate. Some of the energy converted from the mean flow is also transported by diffusion. At stations further downstream, $x/d = 500$, the production and advection terms are returning to the self-preservation values, while diffusion still shows asymmetry. The dissipation at this last station finally shows recognizable asymmetry, being smaller on the unstable side.

The implication of the above observation is important. When the wake undergoes a deflection, the extra or reduced turbulent energy converted from the mean flow takes some time to be transported and dissipated. The present data indicate that the timescales for the responses of the production, diffusion and dissipation are all different. Townsend (1949) estimated that the timescale of mixing in a straight wake is 0.19 $(x-x_0)/U_\infty$, which corresponds to a streamwise mixing distance of about 0.2 $(x-x_0)$. Where x is about $450d$, it is $100d$. In the present Flow A, the streamwise distance between the position where the changes in production are seen ($x/d = 400$), and the position where the dissipation starts showing the effects ($x/d = 500$), is about $100d$. This distance appears to correspond to the mixing scale. It should be noted that the relaxation length discussed by Narasimha & Prabhu (1972) is the distance necessary to return to equilibrium, and is much longer (about $1000d$). It should also be noted that the transverse mixing scale, which represents lengthscales such as the Prandtl mixing length and dissipation length $L_\tau \equiv |\overline{uv}|^{-\frac{3}{2}}/\epsilon$ is much smaller and is about $0.05l_0$. In flows where the changes occur over distances shorter than, or comparable with, this mixing distance the response of ϵ is delayed, and the time- or lengthscale obtained by combining ϵ and velocity scales such as $|\overline{uv}|^{\frac{1}{2}}$ or $(\frac{1}{2}\overline{q^2})$ show both immediate and time-delayed responses. The behaviour of the mixing length and $L_\epsilon = (\overline{q^2})^{\frac{3}{2}}/\epsilon$ is discussed in the next section.

5.3. *On turbulence modelling*

At any level of turbulence modelling, one of the important steps is to express higher-order correlation in terms of lower-order ones. One-point correlations up to fourth order have been measured in the present experiment, and the indications of the data are of interest. In figure 16, the streamwise variations of correlations of different orders are shown. The mean shear strain $\partial U/\partial n - KU$ is also shown, as this is the quantity that is correlated with the second-order correlation $-\overline{uv}$ in an eddy-viscosity-type modelling. The highest-order correlation $\overline{uv^3}$ is the transport of $\overline{uv^2}$, which is the transport of $\overline{uv}$. The maximum absolute values of these quantities are clearly defined in both upper and lower halves of the wake and only these values are plotted. The transverse positions where these values are maximized are different, as can be seen from figures 9(*a*) and 10(*b*), but they are all in the neighbourhood of maximum-shear locations. Incidentally, the position where $\partial U/\partial n - KU = 0$ does not coincide with the position where $\overline{uv} = 0$, and the position where $\partial(\overline{uv})/\partial n = 0$ does not coincide with the positions where $\overline{uv^2} = 0$.

It can be seen clearly from figure 16 that the response of $\overline{uv}$ is very strongly related to the changes in the shear strain $\partial U/\partial n - KU$, but with a definite lag. If one takes the ratio of $\overline{uv}$ and $\partial U/\partial y - KU$ (i.e. the eddy viscosity), it is immediately seen that

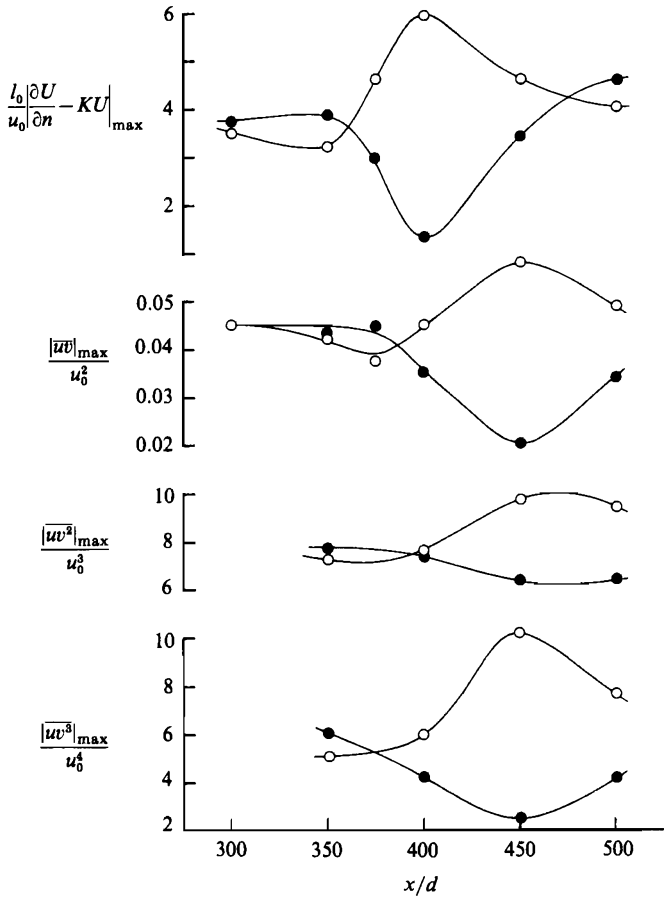

FIGURE 16. The streamwise variation of maximum values of shear strain $\partial U/\partial n - KU$, shear stress $|\overline{uv}|$, the transport of shear stress $\overline{uv^2}$, and $|\overline{uv^3}|$, the transport of $\overline{uv^2}$; ●, upper-half wake; ○, lower-half wake.

at an early station like $x/d = 400$, where $\partial U/\partial y - KU$ on the lower side has dropped to about one-third of the self-preserving value but $\overline{uv}$ has started to drop only about 20%, the eddy viscosity is more than double the self-preserving value. At station $x/d = 450$, where $\overline{uv}$ has decreased to about one-half and $\partial U/\partial y - KU$ has recovered back close to the self-preserving values, the eddy viscosity is now very small. This initial downstream increase and reduction in the eddy viscosity is very large and goes out of phase with the dissipation rate ϵ such that the ratio of eddy viscosity to $(\frac{1}{2}\overline{q^2})^2/\epsilon$, often assumed constant in k–ϵ-type computational methods (e.g. Rodi & Scheuerer 1983), varies widely. The way they change is too complex to be correlated with such parameters as F and S. Simple correction factors applied to mixing length or eddy viscosity based on F or S for slowly changing flows will not work, and methods that reflect both rapid changes and lagged responses will be required. At least simplified transport equations (e.g. Johnson & King 1984) or rate equations are needed.

To demonstrate this, the mixing lengths l_m for Flow A and Flow B are plotted in figure 17 (a, b), and the distribution of the dissipation length L_ϵ is shown in figure 18. The complex behaviour of the mixing-length distributions is seen in figure 17 (a, b).

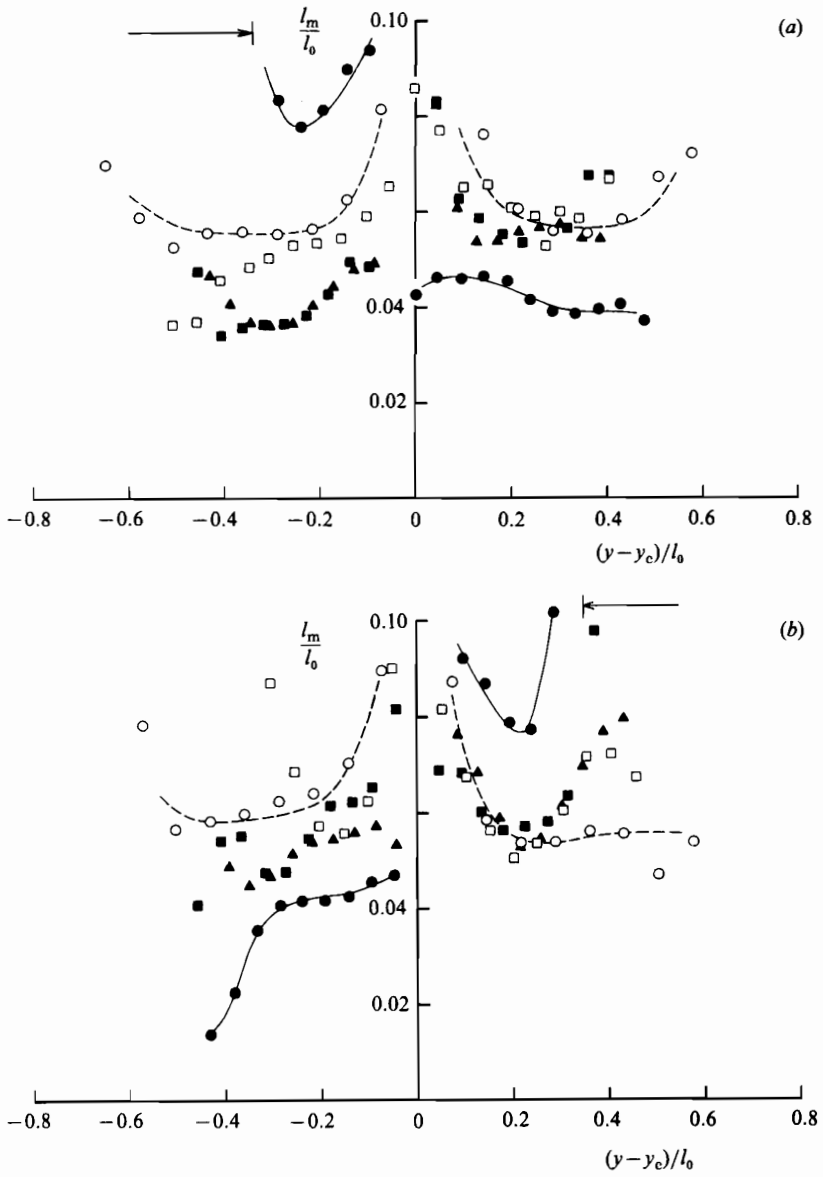

FIGURE 17. Mixing length l_m distributions: (*a*) Flow A, (*b*) Flow B. Symbols are as in figure 7; ↔, region where l_m at $x/d = 400$ is impossible.

To aid in the interpretation of the data, the distribution before the wake deflection is indicated by the broken line and the data points at the strongest-curvature station, $x/d = 400$, are connected by the solid line. In both Flow A and Flow B the mixing length suddenly drops on the unstable side, i.e. the upper half of Flow A and lower half of Flow B, and increases on the stable side. In the outer part of the stable side at $x/d = 400$, the mixing length could not be calculated owing to the negative shear stress in the region of positive shear strain or vice versa. In Flow A, right after the bend, l_m springs back to nearly the original level on the unstable side, while on the

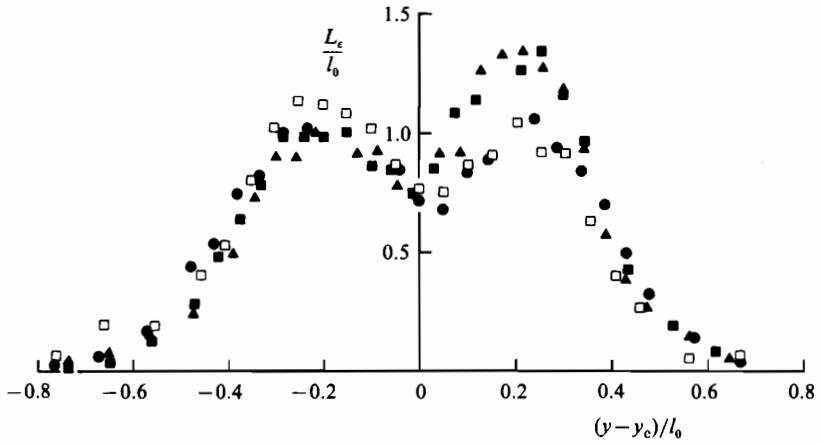

FIGURE 18. Distribution of dissipation lengthscale L_ϵ in Flow A; symbols are as in figure 7.

stable side it jumps down below the initial level and stays there. Similar behaviour is seen in Flow B except l_m goes below the original level on the unstable side. The initial response of l_m at $x/d = 400$ is due mostly to the sudden increase in the shear strain $\partial U/\partial n$, while the initial recovery at $x/d = 450$ is due to the lagged response of $\overline{uv}$ to the change in $\partial U/\partial n$. The initial response of l_m to the application of curvature seen here is an entirely new feature that has not been considered in previous attempts at such boundary-layer modelling (Adams & Johnston 1984; Shizawa & Honami 1983).

The transport equation of the shear stress $\overline{uv}$ contains the transport $\overline{uv^2}$ that needs to be modelled. The response of $\overline{uv^2}$ is seen to be more delayed than $\overline{uv}$. However, the transport $\overline{uv^3}$ of $\overline{uv^2}$ shows a quicker response than $\overline{uv^2}$. Hence, the extrapolation that higher-order correlations inevitably have longer response time does not hold here. It appears that $\overline{uv^3}$ and $\overline{uv}$ have similar timescales.

Figures 19 and 20 illustrate two quantities related to the modelling of the triple product $\overline{u^2v}$. The first quantity is the eddy-diffusivity coefficient C_{tu} for $\overline{u^2}$, defined by

$$C_{tu} \equiv \frac{\overline{u^2v}}{(\overline{q^2}/\epsilon)\,\overline{v^2}(\partial\overline{u^2}/\partial n)}$$

and the second is the turbulent transport velocity V_u, defined by

$$V_u \equiv \frac{\overline{u^2v}}{\overline{u^2}}.$$

It can be seen that C_{tu} behaves in a complicated way and curves are drawn through points to aid visual interpretation. In the central region it was not possible to draw the curves owing to the scatter in the data points. The scatter is due to various errors in the determination of various quantities in the definition of C_{tu}, but the erratic behaviour is also due to the non-coincidence of positions where $\overline{u^2v} = 0$ and $\partial\overline{u^2}/\partial n = 0$. In terms of modelling, the region where $\overline{u^2v} \approx 0$ and $\partial\overline{u^2}/\partial n \approx 0$ is not critically important, so that attention may be concentrated on the values of C_{tu} in the regions where $|\overline{u^2v}|$ takes more than, say, half of the peak values. These regions

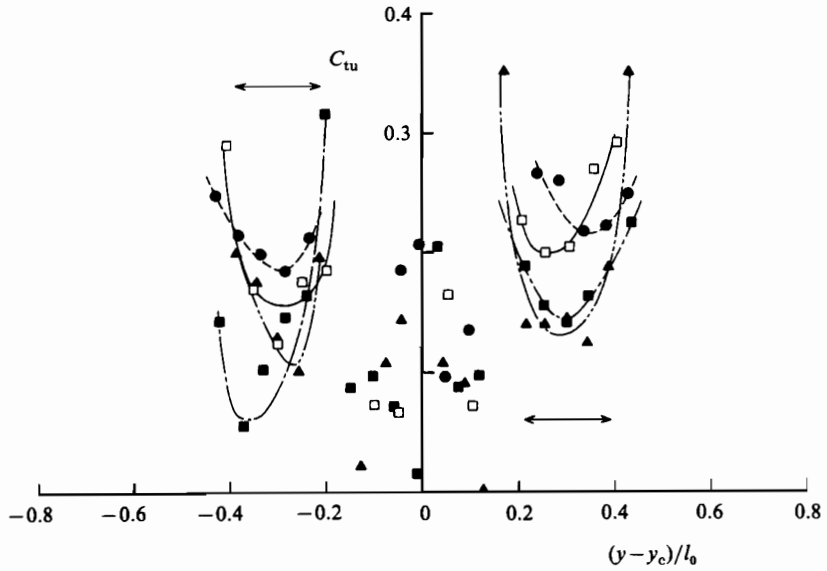

FIGURE 19. The eddy-diffusivity coefficient C_{tu} for $\overline{u^2}$; □–, $x/d = 350$; ●– – –, 400; ■–·–, 450; ▲–··–, 500; ↔, region where $|\overline{u^2v}|$ is significant.

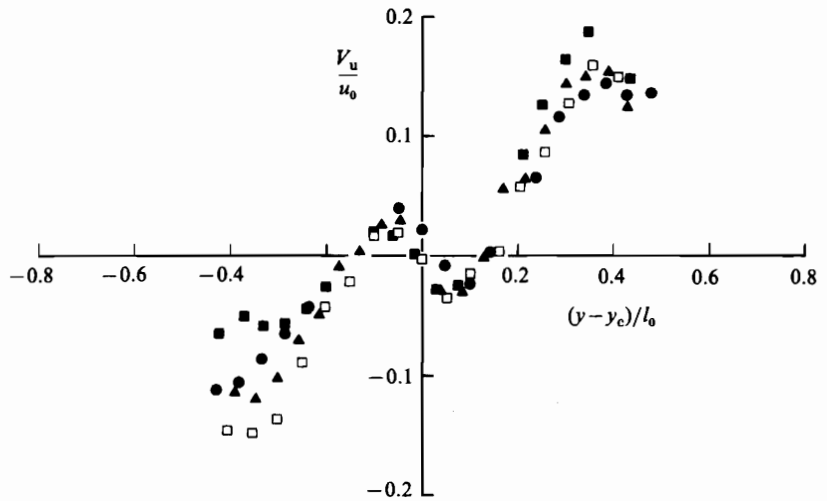

FIGURE 20. The turbulent transport velocity V_u for $\overline{u^2}$; symbols are the same as figure 19.

are indicated by the arrows. It is seen that C_{tu} is reduced on both sides of the wake, but by a larger amount in the lower half. It should be noted that the value of C_{tu} used in the computational method of Launder *et al.* (1975) is 0.21.

The behaviour of the transport velocity V_u is similar to $\overline{u^2v}$, except that it is now 'scaled' by the local value of $\overline{u^2}$. V_u is seen to increase slightly in the (unstable) upper side and decrease in the lower half. The initial drop at $x/d = 400$ is due to the reduced $\overline{u^2}$ there and the low level at $x/d = 450$ and 500 is due mainly to the delayed reductions in $\overline{u^2v}$, similar to that observed with $\overline{uv^2}$ (figure 16).

6. Conclusions

The following main conclusions may be extracted from the preceding text.

Small perturbations in potential flow were found to change greatly the mean strain field of the small-defect wakes so that the shear strain $\partial U/\partial y$ is no longer dominant. Some consequences of thin-shear-layer approximations do not hold and turbulence quantities are strongly influenced by the extra rate of strain.

A simplified form of the momentum equations is recommended for the case of small distortion of small-defect wakes and, if an appropriate definition is made, the equation for defect velocity can be linearized.

Reynolds stresses, particularly the shear stress, are strongly influenced by the streamline curvature and the pressure gradient. The shear stress responds very strongly to changes in the shear strain rate but with a time lag so that such parameters as mixing length behave in a complex manner. The turbulent-kinetic-energy balance was examined in detail. It showed that the production terms respond very quickly but the diffusion terms and the viscous dissipation are delayed. In flows that are changing rather rapidly and are far from equilibrium, non-dimensional parameters formed by different quantities may contain two timescales and may show combinations of rapid and time-delayed responses.

The identification of the features described above makes it important that more basic and systematic investigations of the effects of streamline curvatures on wake flows be undertaken. In particular, further study is required of curved boundary layers with prolonged curvature that may maintain flow in equilibrium, as in the duct flow of So & Mellor (1973).

This work was carried out at the California State University, Long Beach, and was supported by the National Science Foundation Grant MEA-8018565. Thanks are due to Professor H. Unt and Messrs V. Akdag and B. Liu for assistance provided during the measurements and data analysis.

REFERENCES

ADAMS, E. W. & JOHNSTON, J. P. 1984 *Trans. ASME* J: *J. Engng Gas Turbines & Power* **106**, 143.

AKDAG, V., NAKAYAMA, A., LIU, B., KILIK, E. & UNT, H. 1984 Automated hot-wire measurements using a microcomputer. *Mech. Engng Dept Rep.* ME-84-5, California State University, Long Beach.

BRADSHAW, P. 1969 *J. Fluid Mech.* **36**, 177.

BRADSHAW, P. 1973 Effects of streamline curvature on turbulent flow. *AGARDograph* 169.

BRADSHAW, P. 1975 *Trans. ASME* I: *J. Fluids Engng* **971**, 146.

CASTRO, I. & BRADSHAW, P. 1976 *J. Fluid Mech.* **73**, 265.

FABRIS, G. 1979 *J. Fluid Mech.* **94**, 673.

FABRIS, G. 1983 *Phys. Fluids* **26**, 422.

GARTSHORE, I. S. 1967 *J. Fluid Mech.* **30**, 547.

GIBSON, M. M. & RODI, W. 1981 *J. Fluid Mech.* **103**, 161.

GILLIS, J. C. & JOHNSTON, J. P. 1983 *J. Fluid Mech.* **135**, 123.

GUITTON, D. E. & NEWMAN, B. G. 1977 *J. Fluid Mech.* **81**, 155.

HILL, P. G., SCHAUB, U. W. & SENOO, Y. 1963 *Trans. ASME* E: *J. Appl. Mech.* **30**, 518.

HUNT, J. C. R. 1978 *Fluid Dyn. Trans.* **9**, 121.

HUNT, I. A. & JOUBERT, P. N. 1979 *J. Fluid Mech.* **91**, 633.

JOHNSON, D. A. & KING, L. S. 1984 *AIAA paper* 84-0175.

KOYAMA, H. 1983 *Proc. 4th Symp. on Turbulent Shear Flows, University of Karlsruhe, Karlsruhe, F.R. Germany*, p. 6.32.

LAUNDER, B. R., REECE, G. J. & RODI, W. 1975 *J. Fluid Mech.* **68**, 537.

MARGOLIS, D. O. & LUMLEY, J. L. 1965 *Phys. Fluids* **8**, 1775.

MUCK, K. C., HOFFMAN, P. H. & BRADSHAW, P. 1985 *J. Fluid Mech.* **161**, 347.

NARASIMHA, R. & PRABHU, A. 1972 *J. Fluid Mech.* **54**, 1.

RAMAPRIAN, B. R. & SHIVAPRASAD, B. G. 1978 *J. Fluid Mech.* **85**, 273.

RODI, W. & SCHEUERER, G. 1983 *Phys. Fluids* **26**, 1422.

SAVILL, A. M. 1982 *Proc. Int. Symp. on Refined Modelling of Flows, Paris, France*, p. 219.

SAVILL, A. M. 1983 In *Structure of Complex Turbulent Shear Flow* (ed. R. Dumas & L. Fulachier). Springer.

SHIZAWA, T. & HONAMI, S. 1983 *4th Symp. on Turbulent Shear Flows, University of Karlsruhe, Karlsruhe, F.R. Germany*, p. 6.38.

SMITS, A. J. & JOUBERT, P. N. 1981 *J. Ship Res.* **26**, 135.

SMITS, A. J. & WOOD, D. H. 1985 *Ann. Rev. Fluid Mech.* **17**, 321.

SMITS, A. J., YOUNG, S. T. B. & BRADSHAW, P. 1979 *J. Fluid Mech.* **94**, 209.

SREENIVASAN, K. R. 1985 *J. Fluid Mech.* **154**, 187.

SO, R. M. C. & MELLOR, G. L. 1973 *J. Fluid Mech.* **60**, 43.

TOWNSEND, A. A. 1949 *Austral. J. Sci. Res.* **2**, 451.

TOWNSEND, A. A. 1976 *Structure of Turbulent Shear Flows*, 2nd edn. Cambridge University Press.

TOWNSEND, A. A. 1980 *J. Fluid Mech.* **98**, 171.

UBEROI, M. S. & FREYMUTH, P. 1969 *Phys. Fluids* **12**, 1359.